Check for updates

Stress fibres are embedded in a contractile cortical network

Timothée Vignaud [1,2,3], Calina Copos[4], Christophe Leterrier [5], Mauricio Toro-Nahuelpan[6], Qingzong Tseng[1,2], Julia Mahamid [6], Laurent Blanchoin [1,2], Alex Mogilner [4 ✉], Manuel Théry [1,2 ✉] and Laetitia Kurzawa [1,2 ✉]

Contractile actomyosin networks are responsible for the production of intracellular forces. There is increasing evidence that bundles of actin filaments form interconnected and interconvertible structures with the rest of the network. In this study, we explored the mechanical impact of these interconnections on the production and distribution of traction forces throughout the cell. By using a combination of hydrogel micropatterning, traction force microscopy and laser photoablation, we measured the relaxation of traction forces in response to local photoablations. Our experimental results and modelling of the mechanical response of the network revealed that bundles were fully embedded along their entire length in a continuous and contractile network of cortical filaments. Moreover, the propagation of the contraction of these bundles throughout the entire cell was dependent on this embedding. In addition, these bundles appeared to originate from the alignment and coalescence of thin and unattached cortical actin filaments from the surrounding mesh.

Contractile forces are produced mainly by actomyosin bundles or stress fibres in adherent cells[1–3], and by a cortical meshwork of randomly oriented filaments in poorly adherent cells[4,5]. The mechanism regulating the production and transmission of local forces throughout the cell is still poorly understood[6–8]. The progress in understanding this integration process has notably been limited by the technical challenges to manipulate the network locally while simultaneously measuring the impact on force production at the level of the entire cell.

Stress fibres are formed by the interaction and merging of pre-existing radial fibres and transverse arcs[9–12]. Transverse arcs are formed by the alignment and compaction of filaments at the cell front, as they are pulled by the actin network retrograde flow against cell anchorages[13,14]. As a result, actomyosin networks are composed of interconnected contractile elements that span the entire cytoplasm and serve as a template to transmit mechanical forces over long cellular distances[15–17]. Laser photoablation experiments have indeed demonstrated that the photoablation of a single stress fibre could compromise the entire traction force field[18,19] and lead to variations in tension in all focal adhesions including those that are not at the ends of the ablated fibres[20]. Similarly, stretching cells unidirectionally can lead to a tension increase in all focal adhesions whatever their orientation[21]. Hence, directional forces along specific actomyosin bundles can propagate to other bundles with which they are interconnected. As a consequence, the tension in a stress fibre does not only depend on forces produced in that fibre but also on the connection and orientation of adjacent fibres[22]. This high degree of connection between actomyosin bundles can provide mechanical coherence at the level of the cell[23–25]. However, it is yet unclear how forces are transmitted from one stress fibre to another.

Theoretical models of contractile networks have proposed two main paradigms to capture the mechanisms of force production and transmission in cells. In one paradigm, discrete models, that include high-level details on the structure of the network, offer an accurate description of the stress fibre as a load-bearing structure and of the traction forces exerted on its anchorages to the extra-cellular matrix[26–30]. These models are successful at providing a description in fine detail of local force production, but fail to provide a global description of the traction force field. In the other paradigm, continuous models provide a more global view of the contractile networks by incorporating only a few coarse-grained biophysical parameters. These models work well for describing force variations with changes in cell size and shape[31–33], but require focal adhesions to be taken into account to be more accurate[34]. These considerations suggest that the limitations of the discrete and the continuous models could be overcome by developing an intermediate model that takes into account both features of the network.

Results

Cells with stress fibres produce high contractile forces. We first tested experimentally if the presence of actin bundles could impact the magnitude and distribution of traction forces as compared to a more homogeneous network of the same size and shape[32,33]. To that end, cells were plated on either dumbbell-shaped or pill-shaped micropatterns fabricated on a polyacrylamide hydrogel. The size of the micropatterns, 60 μm long, corresponded to the average length of cells on a polyacrylamide gel homogeneously coated with fibronectin (Extended Data Fig. 1a–c). The dumbbell-shaped micropattern was designed to promote in the cell the assembly of two stress fibres, which are known to form preferentially above the non-adhesive zone[35,36], whereas the pill-shaped micropattern was

[1]CytoMorpho Lab, Interdisciplinary Research Institute of Grenoble, Laboratoire de Physiologie Cellulaire et Végétale, Grenoble-Alpes University/CEA/CNRS/INRA, Grenoble, France. [2]CytoMorpho Lab, Hôpital Saint Louis, Institut Universitaire d'Hématologie, Université Paris Diderot/CEA/INSERM, Paris, France. [3]Clinique de Chirurgie Digestive et Endocrinienne, Hôtel Dieu, Nantes, France. [4]Courant Institute and Department of Biology, New York University, New York, NY, USA. [5]NeuroCyto, Institute of NeuroPhysiopathology (INP), CNRS, Aix Marseille Université, Marseille, France. [6]Structural and Computational Biology Unit, European Molecular Biology Laboratory (EMBL), Heidelberg, Germany. ✉e-mail: mogilner@cims.nyu.edu; manuel.thery@cea.fr; laetitia.kurzawa@cea.fr
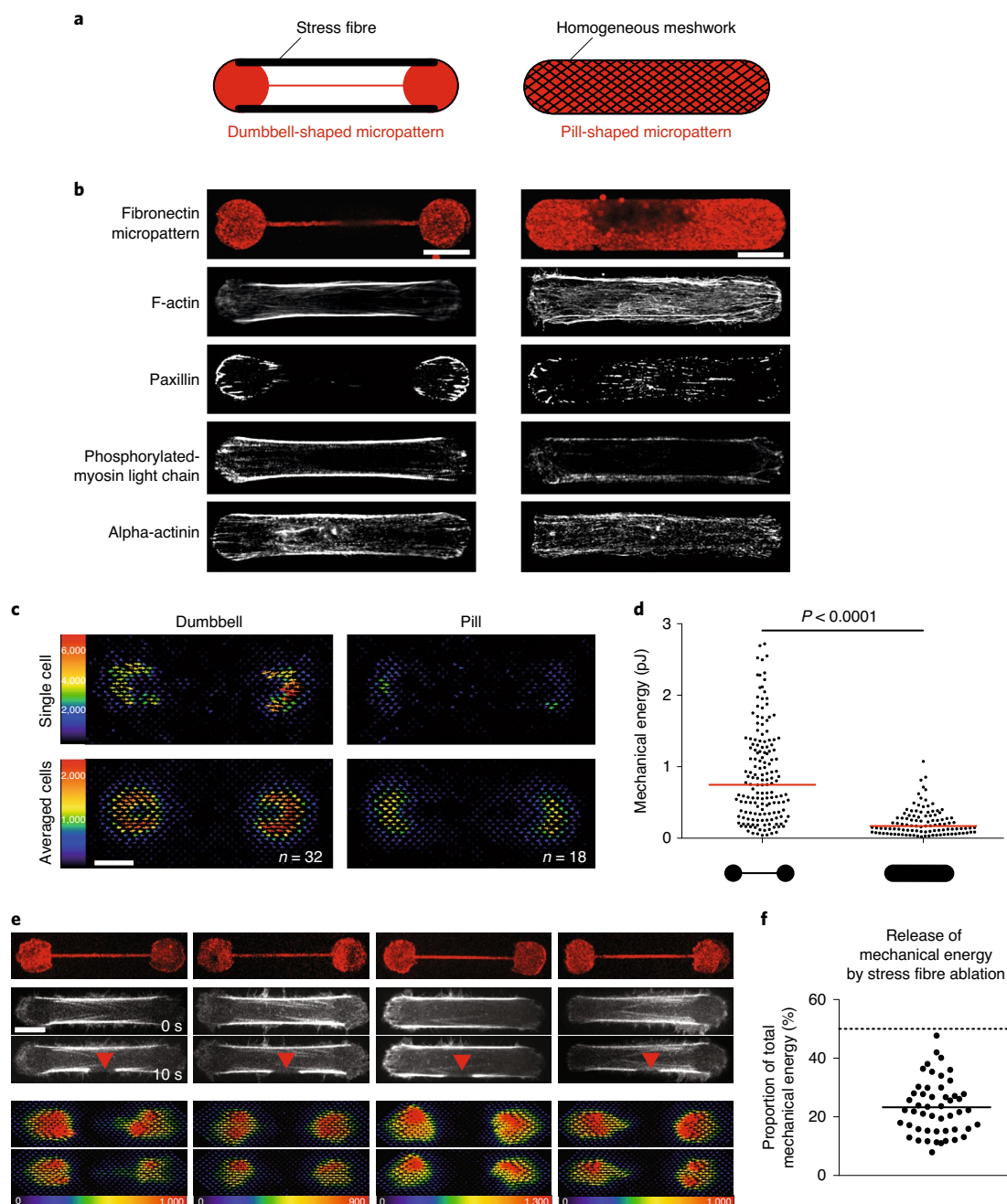
Fig. 1 | The stress fibre sets the magnitude of the traction force exerted by the cell but remains under tension after photoablation. a, Micropattern designs (60 μm length) and their respective outcomes in the actin-network architecture. Dumbbell shape (left): actin stress fibres (thick black lines) form between the two adhesive discs (red). Pill shape (right): formation of a continuous actin mesh. **b**, Immunostainings of RPE1 cells spread on dumbbell-shaped (left panel) and pill-shaped (right panel) polyacrylamide micropatterns. For each shape, single examples of representative cells are displayed. From top to bottom, micropattern labelling (fibrinogen–Cy5); actin (phalloidin Atto 488); paxillin (Alexa Fluor 488); phosphorylated-myosin light chain (Cy3); and alpha-actinin (Cy3). Image scale bars, 10 μm. $N = 3$ independent experiments. **c**, Traction force maps of cells spread on dumbbell (left column) and pill (right column) micropatterns of 37 μm. Upper images display traction force maps of single representative cells. Lower images show averaged traction force maps of cells. Scale colour bars in pascal. Image scale bar, 7 μm. **d**, Scatter plot of the mechanical energies of single cells and associated P value (two-tailed Mann–Whitney t-test, $P < 0.0001$, median is depicted). Dumbbell shape, $n = 160$ cells, $N = 7$ experiments; pill shape, $n = 107$ cells, $N = 2$ experiments. **e**, Force relaxation study upon peripheral stress fibre photoablation. Left panel from top to bottom, micropattern labelling (fibrinogen–Cy5); actin (LifeAct-GFP) before photoablation (0 s) and after photoablation (10 s, red arrow); corresponding traction force maps of the initial forces; and traction force maps after photoablation. Image scale bar, 10 μm. Force scale colour bar in pascal. $N = 4$ experiments. **f**, Scatter plot of individual released mechanical energies after stress fibre photoablation (percentage of the initial mechanical energy) for $n = 50$ cells, $N = 4$ experiments. Mean is depicted.

designed to promote a more homogeneous network of actin filaments (Fig. 1a). Both micropatterns were devised to promote the cells adopting the same shape.

As expected, two main peripheral stress fibres and only a few smaller and thinner internal bundles were formed in cells plated on dumbbell-shaped micropatterns. These structures were localized in

the ventral side of the cells and concentrated the cross-linkers of actin filaments and myosins[37]. By contrast, numerous, more evenly distributed but thinner bundles of actin filaments were formed in cells on pill-shaped micropatterns (Fig. 1b and Extended Data Fig. 1e). The contractility generated by these cells forming two distinct cytoskeletal networks enclosed in a similar envelope was measured using traction force microscopy. As illustrated by the averaged traction force maps and quantified by the mechanical energy that was transferred to the hydrogel, significantly higher mechanical energy was generated by cells containing the stress fibres (dumbbell micropattern) than the cells without (pill micropattern; Fig. 1c,d). Similar changes were observed with other micropattern geometries in which the modulation of the size and position of non-adhesive zones affected the production of stress fibres (Extended Data Fig. 1d). This result indicated that the organization of actomyosin components into stress fibres, in response to local variations of substrate adhesiveness, plays a major role in setting the magnitude of force a cell could generate and transmit to the substrate. However, these global force measurements could not reveal the quantitative contribution of individual stress fibres to the total force produced by the cells.

Stress fibres are connected to surrounding actin network. By combining photoablation of the peripheral stress fibres with traction force measurements, we assessed the specific contribution of these fibres to the global mechanical energy produced by cells plated on dumbbell micropatterns. A stress fibre was severed mid-length by localized pulsed-laser photoablation at 355 nm (Supplementary Video 1), and the release in fibre tension was captured by the relaxation in the hydrogel substrate (Fig. 1e and Supplementary Video 2). Surprisingly, the released energy from the cut of one of the two peripheral stress fibres was about 25% of the total mechanical energy generated by the cell (Fig. 1e,f), and was substantially lower than the expected 50%, which assumes the two peripheral stress fibres generate most of the mechanical energy.

This prompted us to investigate in more detail the relaxation of the severed stress fibre. Marks were photobleached along the fibre to monitor the entire relaxation pattern after the severing[38] (Fig. 2a). As previously described, the retraction of a severed end was characteristic of a viscoelastic relaxation[19,39,40] (Fig. 2b). To characterize the retraction, the normalized retraction distance was calculated by dividing the length of each retracted segment (between two marks) by its initial length. Corresponding retraction values were plotted as a function of the initial distance of the photobleached segment from the photoablation site (Fig. 2c). Twenty-two negative values were excluded from the analysis as corresponding to cells in which the photoablation was not efficient. The parts of the fibre distal to the photoablation displayed minimal if any relaxation (Fig. 2b,c), and contrasted with what would be expected with a stress fibre in isolation, in that the relaxation should be independent of the distance from the photoablation (Fig. 2c). Hence, this result suggested that the fibre was not isolated but connected along its length to force-bearing elements that resisted the deformation when the fibre was severed. Similar observations have been made elsewhere in cells spread on a uniform extra-cellular matrix coating[38]. In this work, stress fibres appeared to be connected to the extra-cellular matrix via focal adhesion-like complexes that acted as elastic linkers, and were shown to accumulate zyxin at their severed ends following photoablation at locations where new adhesions were formed. However, with the dumbbell micropattern, stress fibres were above a non-adhesive substrate, precluding the possibility of transmembrane adhesions forming at the severed ends. This led us to hypothesize that peripheral stress fibres were not connected to the extra-cellular environment but to cortical actin filaments.

Cut stress fibres are still under tension. Importantly, and in contrast to the classical view of stress fibres pulling on focal adhesions

only, the stress fibre connection to adjacent actin cytoskeletal elements implied that photoablation should redistribute the tension of the fibre to the surrounding meshwork. As a result, the remaining parts of the severed fibre should still be under tension. To test this prediction, two photoablations were performed sequentially less than a minute apart on the same fibre. In confirmation of the prediction, a noticeable release of energy, calculated as the percentage of the mechanical energy before photoablation, was associated with the second photoablation (Fig. 2d). However, the amount of energy that was released by the second photoablation was much lower than the first one because the severed fibre had already relaxed and lost some of its elastic energy. To investigate whether this lower amount of energy release resulted from a non-specific injury to the cell due to the photoablations, the second photoablation was performed on the other intact fibre. In that case, approximately the same amount of energy was released as that after the first photoablation, showing that the first photoablation did not impact cell integrity (Fig. 2e).

Previous work has suggested that discrete connections of a peripheral stress fibre to other internal fibres can affect the fibre's relaxation pattern after severing[22,41]. However, as opposed to these descriptions, the incomplete relaxation pattern of the severed peripheral stress fibres we observed in our work was not systematically associated with interconnections with internal fibres, as illustrated by the absence of visible fibres connected to the peripheral stress fibres in Fig. 2a. This led us to hypothesize that a stress fibre was connected to a low-density and widespread actin meshwork. This hypothesis was addressed by disconnecting the stress fibre from the meshwork through photoablation of a narrow region medial and parallel to the length of the fibre above the non-adhesive substrate on the hydrogel (a process we termed fibre shaving; Fig. 2f and Supplementary Video 3). With two successive photoablations performed along the stress fibre, the release of energy after the second photoablation was significantly lower when the fibre had been shaved first (Fig. 2g,h), supporting the hypothesis that low-density fibres connections to the peripheral stress fibre prevented the complete relaxation of the stress fibre after it was severed.

Modelling the stress fibres embedded in an elastic meshwork. To investigate the properties of such a network of actin fibres embedded in a cortical meshwork, we built on the ideas developed in the literature[28,38] to create a new biophysical model. In this model, and in contrast with previous ones, the stress fibres were not connected to the extra-cellular matrix but to the adjacent cortical meshwork. The cortical meshwork was described as a two-dimensional (2D) ensemble of elastic links connected by nodes. The stress fibres were modelled as elastic links under tension and connected in series. The stress fibres were connected uniformly along their length to the cortical meshwork by elastic links (Fig. 3a; described in detail in the Supplementary Methods).

We first tested the response of our model to fibre severing by locally reducing the stiffness by 90% in one of the stress fibre elements (Fig. 3b). As in the experimental set-up, mechanical energy was released but was substantially less than 50%, even though in the model, it was exclusively produced by the two peripheral fibres (Fig. 3b). The model also accurately accounted for the limited retraction of the fibre at distal points from the site of the simulated photoablation (Fig. 3c). Furthermore, the model captured the additional release of energy after a second photoablation of the same fibre (Fig. 3d).

Other experimental observations prompted further investigations of the model. In the experimental set-up, the release in tension was not equivalent on the two severed parts of the stress fibre, and was not restricted to its distal ends; rather, the release in tension appeared higher at the end that was closer to the photoablation and extended to the other side of the cell (Fig. 3e and other examples in
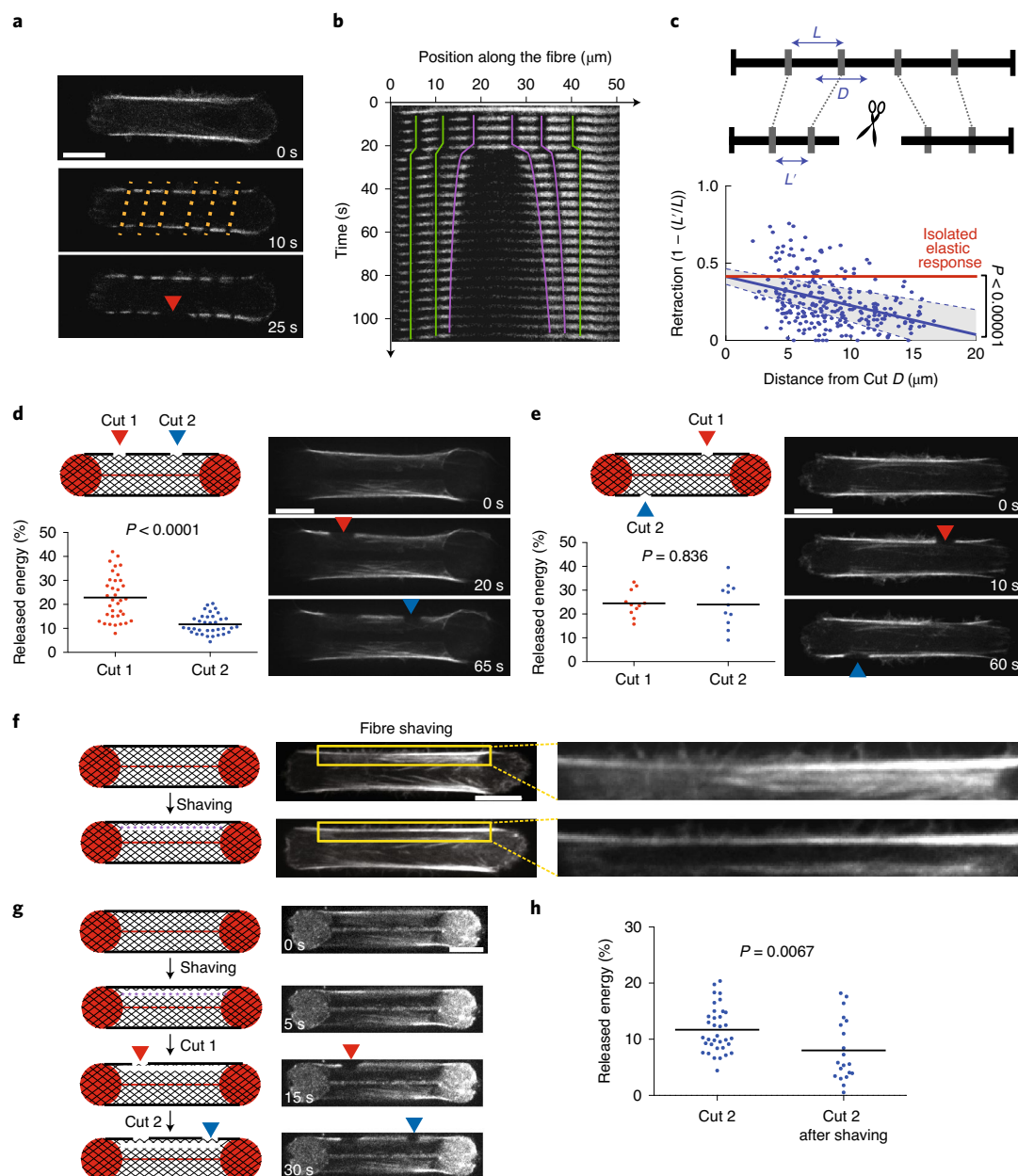
Fig. 2 | Stress fibres are connected to the surrounding actin cytoskeletal network. a, From top to bottom, RPE1–actin-GFP time-lapse images. Stripes added by photobleaching (10 s, orange dashed lines); cut by photoablation (25 s, red arrow). Image scale bar, 10 μm. $N = 2$ experiments. **b**, Corresponding kymograph (coloured lines highlight the retraction of the photobleached marks). **c**, Normalized retraction distance as a function of the initial distance of the photobleached segment from the photoablation site ($n = 264$ segments; 44 cells analysed from two experiments). L and L' represent the length of a segment in between two photobleached marks, respectively, before and after photoablation; and D represents the distance of retraction of the segment from the cut site following ablation. Blue line corresponds to the linear regression minimizing squared error; 95% confidence intervals (-0.0243, -0.0132 indicated by the grey area) based on standard errors indicate a negative slope that is distinct from zero (isolated elastic fibre, $P < 0.00001$, two-tailed t-test). **d**, Two sequential cuts on the same stress fibre (Cut 1, red arrow; Cut 2, blue arrow). Time-lapse images of RPE1–LifeAct-GFP cells after the two sequential photoablations. Scatter plots of the released mechanical energy (mean is depicted) for the two photoablations ($n = 35$ cells, $N = 3$ experiments). P value from a two-tailed paired t-test is indicated on the plot ($P < 0.0001$). Image scale bar, 10 μm. **e**, Two sequential cuts on the two stress fibres in the cell (Cut 1, red arrow; Cut 2, blue arrow). Time-lapse images of RPE1–LifeAct-GFP cells after two photoablations. Scatter plots of the released mechanical energy for the two types of photoablation ($n = 11$ cells, $N = 1$ experiment, mean is depicted). P value from a two-tailed paired t-test is indicated on the plot ($P = 0.836$). Image scale bar, 10 μm. **f**, Stress fibre shaving. The shaved region (illustrated on the scheme by the star-shaped dotted line and corresponding to the dark area in the images) is highlighted in the yellow inset and corresponding zoomed-in images. Image scale bar, 10 μm. **g**, Shaving (purple star-shaped dotted line) followed by two sequential cuts on the adjacent peripheral stress fibre (Cut 1, red arrow; Cut 2, blue arrow). RPE1 cells labelled with SiR-actin and corresponding micropatterns (fibrinogen–Cy5) in a time sequence corresponding to the shaving ($t = 5$ s), the first photoablation ($t = 15$ s, red arrow) and the second photoablation ($t = 30$ s, blue arrow). Image scale bar, 10 μm. $N = 3$ experiments. **h**, Scatter plot of the mechanical energy released by the second photoablation of the stress fibre alone (Cut 2; $n = 35$ cells, $N = 3$ experiments) or preceded by a shaving (Cut 2 after shaving; $n = 20$ cells, $N = 4$ experiments). Means are depicted. P value from two-tailed unpaired t-test is indicated on the plot ($P = 0.0067$). Eight negative values were excluded from the analysis as corresponding to cells in which the photoablation was not efficient.
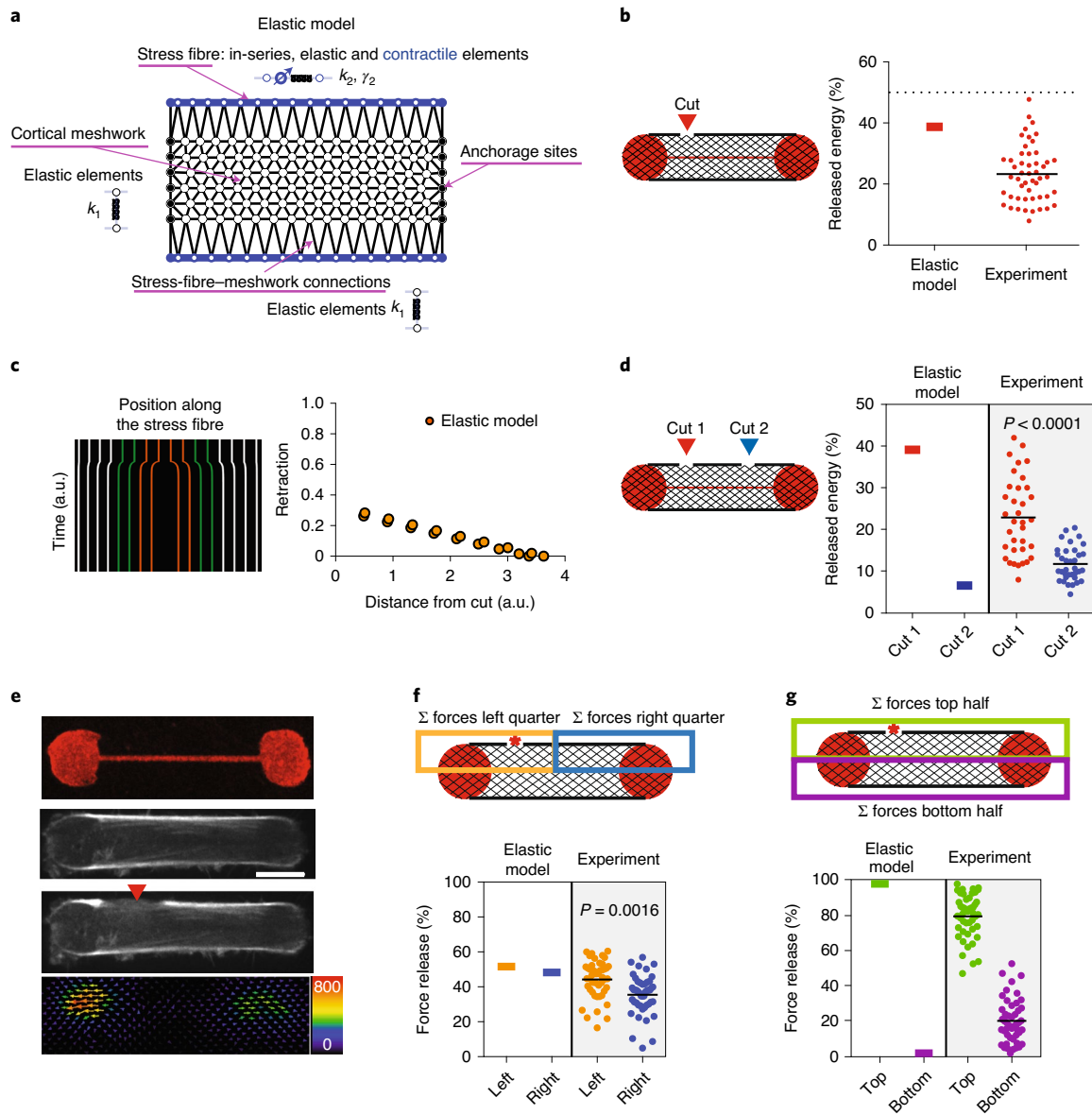
Fig. 3 | Model with active contractile stress fibres embedded in an elastic central mesh. a, Diagram illustrating all components in the model, including the isotropic elastic cortical mesh, contractile elastic fibres along the long edges of the mesh and adhesive sites located along the short edges of the mesh (κ_1 and κ_2 represent the stiffnesses of the springs in the meshwork and stress fibres, respectively; γ_2 represents the tension in the stress fibres). **b**, Plot displaying simulated traction force loss as a result of the stress fibre ablation and corresponding experimental data. $n=50$ cells, mean is depicted. **c**, Simulated kymograph of a stress fibre indicating the movement of the regularly spaced markers after simulated photoablation. Plot of the associated normalized retraction of these markers as a function of the distance from the ablation site. **d**, Predicted and experimental mechanical energy release after two sequential photoablations on the same stress fibre. $n=35$ cells, $N=3$ experiments, mean is depicted. P value from a two-tailed paired t-test is indicated on the plot ($P<0.0001$). **e**, Representative image of the dumbbell-shaped micropattern (fibrinogen–Cy5) and RPE1-LifeAct-GFP cells displaying photoablation at a lateral side of the stress fibre (red arrow) and the associated relaxation traction force field after the photoablation. Image scale bar, 10 μm. Force scale colour bar in pascal. $N=3$ experiments. **f**, Spatial distribution of force relaxation along the stress fibre after stress fibre photoablation (red star). Top panel: the release of traction forces was calculated in partitioned area of the cell, where the orange zone included half the stress fibre and the off-centred photoablation site, and the blue zone included the other half of the stress fibre. Forces were summed within each defined zone as indicated by the Σ symbol. Bottom panel: plot displaying the prediction of the model and the experimental measurements ($n=47$ cells, $N=4$ experiments, mean is depicted) for the magnitude of released forces with respect to these zones. P value from the two-tailed paired t-test is indicated on the plot ($P=0.0016$). **g**, Spatial distribution of force relaxation across the cell after stress fibre photoablation (red star). Top panel: the release of traction forces was calculated in partitioned area of the cell, where the green zone included the stress fibre with photoablation site, and the purple zone included the stress fibre without photoablation. Forces were summed within each defined zone as indicated by the Σ symbol. Bottom panel: plot displaying the prediction of the model and the experimental measurements ($n=47$ cells, $N=4$ experiments, mean is depicted) for the magnitude of released forces with respect to these zones.

Extended Data Fig. 2). By contrast, an isolated stress fibre would be expected to release the same amount of tension at both ends. This suggested that the cortical meshwork had an impact not only on the magnitude but also on the spatial distribution of traction force production. To quantify this spatial effect in the model, the cell area was partitioned into four quadrants, and the relative traction force loss

was measured in each quadrant as a percent amount of total traction force loss in the cell (Fig. 3f,g). Intriguingly, the model could barely account for the asymmetric traction force loss at the end of the severed stress fibre (Fig. 3f), and no traction force loss occurred on the other side of the cell where the stress fibre was intact (Fig. 3g). In addition, although we could define a given set of parameters for network elasticity that could account qualitatively for the various trends of traction force relaxation, the traction force changes were only in limited quantitative agreement with the equivalent experimental measurements (Fig. 3b,d,f,g). Puzzled by the discrepancy between the predictions of the model and the measured loss of traction force on the other half of the cell after fibre photoablation, we decided to further interrogate the mechanical nature of the cortical meshwork.

The cortical meshwork is contractile. A local ablation in the cortical meshwork did not release an important amount of energy as compared to the same ablation in a peripheral stress fibre (Extended Data Fig. 3a). However, the shaving of a stress fibre, that is, the longitudinal photoablation of the cortical meshwork, led to a notable release of contractile energy, calculated as the percentage of the total mechanical energy before photoablation (Fig. 4a,b). This release was comparable to that of fibre ablation. This result showed that the cortical meshwork was contractile and not passively elastic as initially hypothesized. It also meant that the cortical meshwork actively participated in the production of traction forces. Indeed, the release of mechanical energy after a single ablation and the release of mechanical energy after shaving of the stress fibre were additive (Fig. 4a,b and Supplementary Video 4), and consistent with the theoretical expectation, these photoablations disrupted half of the contractile network (Fig. 4a). The contractility of the cortex could also be revealed by impairing its branched architecture. The chemical inhibition of actin-related proteins-2/3 (ARP2/3) complex increased the global cell contractile energy although it did not affect the amount of energy released by peripheral fibre ablation, suggesting that the global increase was specifically due to the reorganization of the cortex (Extended Data Fig. 3b). Furthermore, moving the position of the bar of the dumbbell shape did not affect the peripheral fibres, but changed the area of the cortex they were connected to. As a result, the fibre associated with a larger part of the cortex released more energy when ablated, further showing that the cortex contributed to the production of force along the fibre (Extended Data Fig. 3c).

Hence, we revised our initial elastic model by including contractility as a function of the cortical mesh (Fig. 4c). The links in the cortical mesh were thus considered as contractile cables, that is, tensed elastic springs in series with contractile elements (Fig. 4c). In this second contractile model, the spring constants and contractilities of the cortical-mesh and fibre-mesh links were the same, and different from those characterizing the stress fibres. The estimations of the magnitude and localization of mechanical energy release based on this contractile model were in better agreement with the experimental data, including that the contractile energy released after stress fibre ablation was lower than in the elastic model (Fig. 4d) and that the contractile energy released after stress fibre shaving was higher than in the elastic model (Fig. 4e). As with the elastic model, the contractile model accounted correctly for the difference in contractile-energy release after the second photoablation whether it was applied to the same or opposite stress fibre. However, the amount of contractile energy released in these scenarios was in better agreement with experimental data with the contractile model than with the elastic model (Fig. 4f,g). More importantly, the contractile model captured key features of the spatial distribution of traction force loss in response to a single photoablation in contrast to the elastic model. The contractile model recapitulated the asymmetry of traction force loss at both ends of the severed fibres (Fig. 4h) and the important traction force loss registered on the opposite side of the cell (Fig. 4i). In addition, with the scenario of shaving the stress fibre prior to an off-centre photoablation of that fibre (Extended Data Fig. 4a), the contractile model, in comparison with the elastic model, better accounted for the left–right symmetrical loss of traction force (Extended Data Fig. 4b), and captured the loss of traction force at the opposite side of the cell (Extended Data Fig. 4c).

The theoretical modelling combined with the experimental observations supported the hypothesis that the stress fibres and the cortical meshwork were mechanically similar in that they were both elastic and contractile. Therefore the stress fibres and the cortical meshwork may not be distinct networks with discrete interconnections, but part of a single integrated network, in which architecture and mechanics of actomyosin arrays vary in space.

The cortical meshwork forms a continuum with stress fibres. To investigate further the physical interplay between stress fibres and the cortical meshwork, fixed cells were imaged at the resolution

Fig. 4 | The cortical meshwork is contractile. a, Scatter plot of the released mechanical energy after shaving (left; $n = 94$ cells, $N = 14$ independent experiments), single cut (centre; $n = 50$ cells, $N = 4$ independent experiments) or cut after shaving (right; $n = 65$ cells, $N = 14$ independent experiments). P values from two-tailed unpaired t-tests ($P = 0.0074$ for single cut versus shaving; $P < 0.0001$ for single cut versus cut after shaving). Nineteen outliers were removed from the analysis (using the remove outliers function of Prism). **b**, Left panel: RPE1–LifeAct-GFP cell images depicting a stress fibre subject to shaving (performed in between two red stars), single cut (red arrow), and cut after shaving conditions (bottom image). Right panel: corresponding traction force maps. The same cell was represented to illustrate shaving and cut after shaving (top and bottom panels, respectively). Image scale bar, 10 μm. Force scale colour bar in pascal. $N = 3$ experiments. **c**, Diagram illustrating all components in the fully contractile model, including an isotropic contractile cortical mesh. **d**, Mechanical energy released after stress fibre photoablation (red arrow). Plot displaying the predictions of the elastic and contractile models and the experimental measurements for which mean is depicted ($n = 50$ cells). **e**, Mechanical energy released after shaving (purple star-shaped dotted line). Plot displaying the predictions of the elastic and contractile models and the experimental measurements for which mean is depicted ($n = 94$ cells, $N = 14$ experiments). Nine outliers were removed from the plot (using the remove outliers function in Prism). **f**, Sequential cuts on the same stress fibre (Cut 1, red arrow; Cut 2, blue arrow). Predictions of the elastic and contractile models and experimental data for which means are depicted ($n = 35$ cells, $N = 3$ experiments). P value calculated from a two-tailed paired t-test. **g**, Sequential cuts on the two stress fibres in the cell (Cut 1, red arrow; Cut 2, blue arrow). Predictions of the elastic and contractile models and experimental data for which means are depicted ($n = 11$ cells, $N = 1$ experiment). P value calculated from a two-tailed paired t-test. **h**, Spatial distribution of force loss along the stress fibre after off-centre stress fibre cut (red star). The loss of traction forces was calculated in partitioned area of the cell: the orange zone included half the stress fibre and the off-centred photoablation site, while the blue zone included the other half of the stress fibre. Forces were summed within each defined zone as indicated by the Σ symbol. Plot displaying the prediction of the elastic and contractile models and the experimental data for which means are depicted ($n = 47$ cells). P value calculated from a two-tailed paired t-test is indicated on the plot ($P = 0.0016$). **i**, Spatial distribution of force loss after off-centre stress fibre photoablation (red star) in partitioned area of the cell where the green zone included the stress fibre with photoablation site, and the purple zone included the stress fibre without photoablation. Forces were summed within each defined zone as indicated by the Σ symbol. Plot displaying the prediction of the elastic and contractile models, and the experimental data for which means are depicted ($n = 47$ cells).

of single actin filaments by cryo-electron tomography (Cryo-ET) of micropatterned cells[42]. This imaging revealed that stress fibres were connected via multiple filaments to the meshwork that covers the plasma membrane (blue arrows in Fig. 5a). Stress fibres did not appear as an isolated structure but instead formed a continuous structure with the cytoplasmic meshwork (Fig. 5b, Extended Data Fig. 5 and Supplementary Video 5). The density of filaments decreased progressively from the inner part of the fibre to the cytoplasmic meshwork (blue arrows in Fig. 5b). Fine intracellular architectures were also analysed by stochastic optical reconstruction

microscopy (STORM). Instead of two distinct networks on top of each other, the imaging revealed that stress fibres were fully entangled in the cortical meshwork. In the cortex, filaments formed bundles that were progressively more longitudinally aligned with closer proximity to the peripheral stress fibre (Fig. 5c). Similar continuous architectures, with progressive alignment of cortical filaments in the cortex up to their interlacing with the bundles forming the stress fibres, were also observed with STORM in other cell types and in the absence of an adhesive micropattern (Fig. 5d). In particular, the zoomed-in view of the astrocyte shows several bundle sizes in the
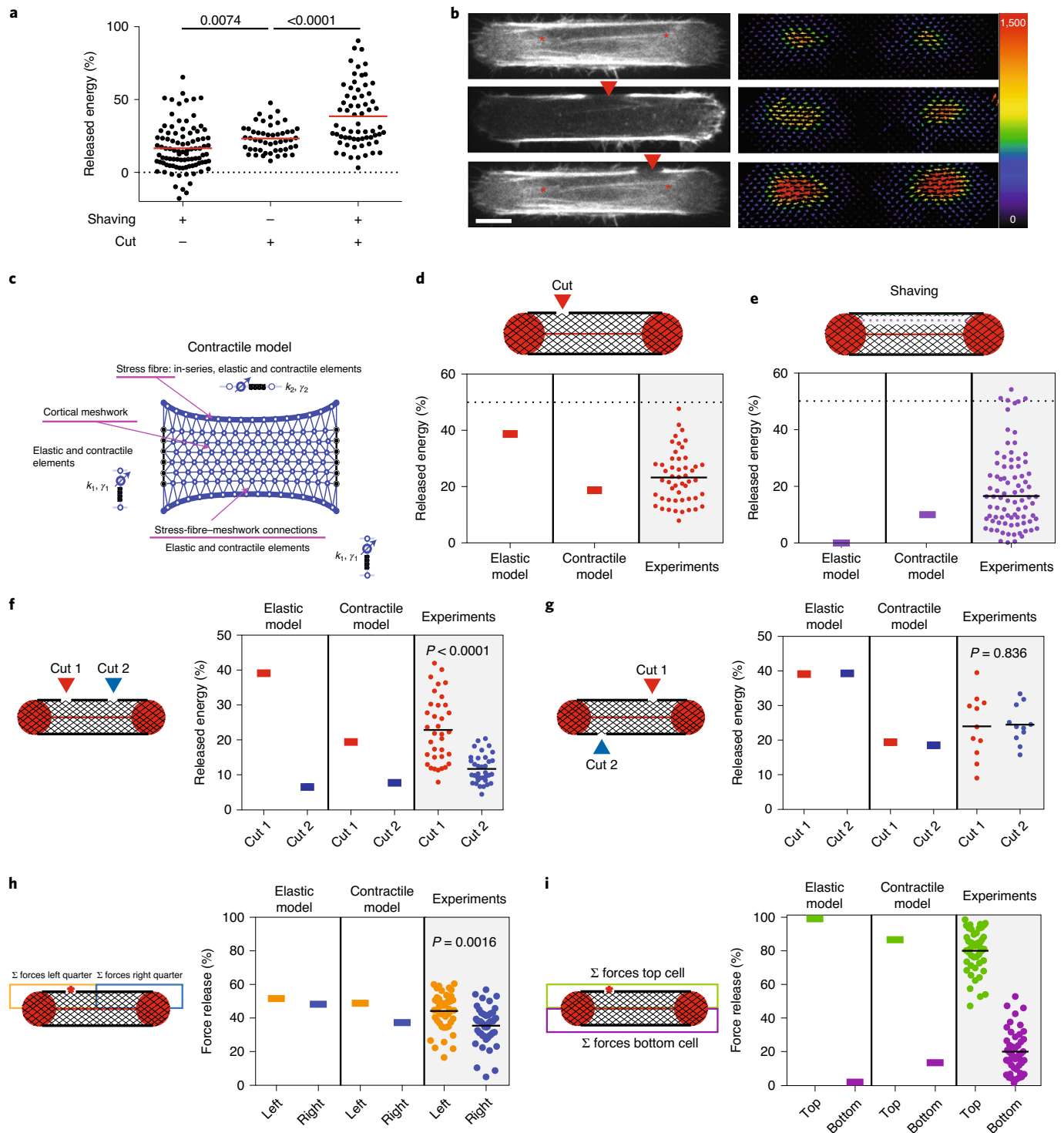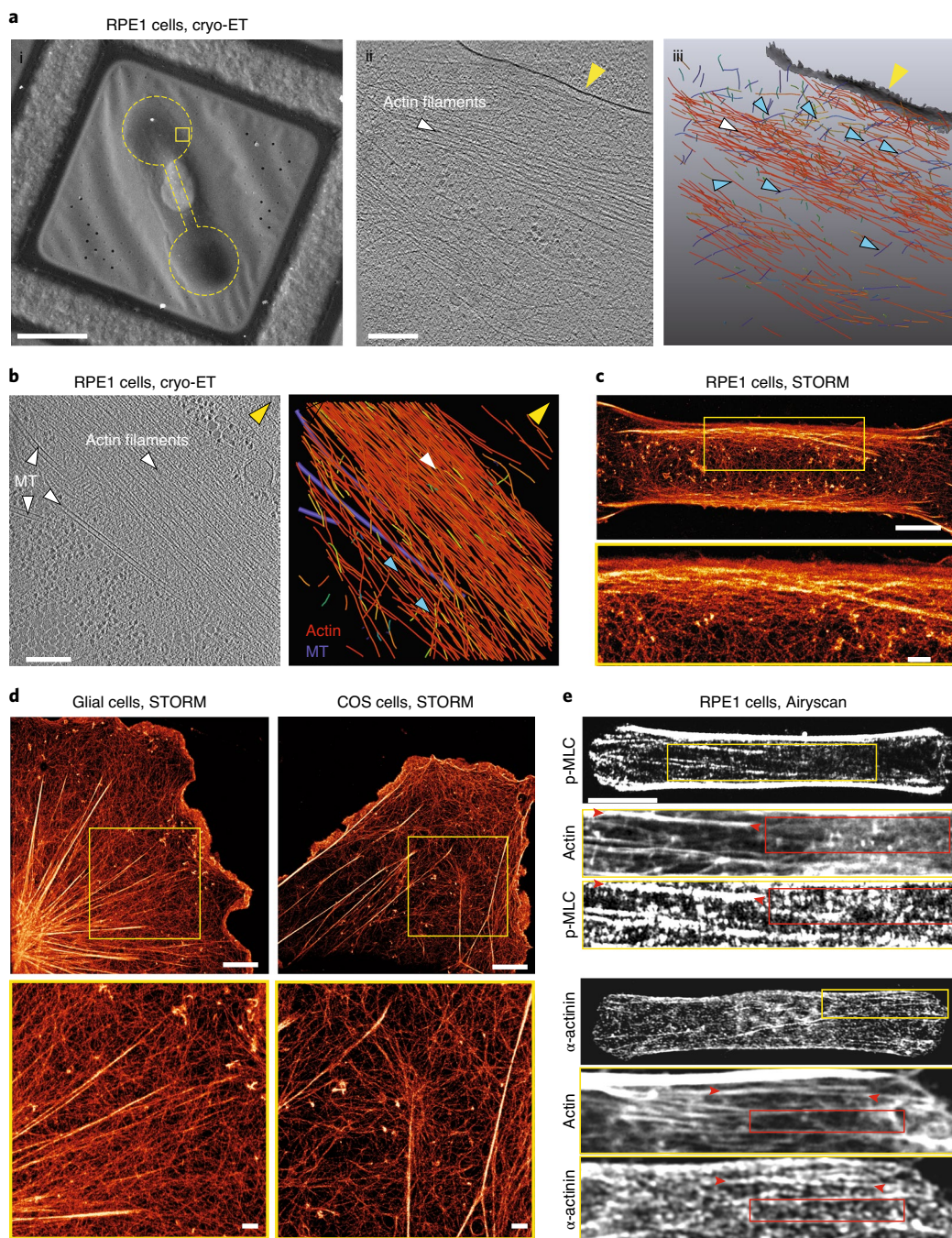
Fig. 5 | The stress fibre is fully embedded in the adjacent actin cortex. a, (i) Cryo-ET of a vitrified RPE1 cell adhered on a dumbbell-shaped micropattern. Yellow rectangle, putative location of the acquired tomograms. Yellow dashed line, dumbbell-shaped pattern's size and position. Scale bar, 20 μm. (ii) Tomographic slice (6.8 nm thickness) in a second cell. Scale bar, 200 nm. Yellow arrow, plasma membrane; white arrow, actin filaments forming a bundle. (iii) Perspective view of the three-dimensional (3D) rendering of the actin filament network from (ii). Blue-to-red colour map of actin filaments shows angular distribution (ranging from 0° to 90°) relative to the z plane of the tomogram. Grey, plasma membrane. Blue arrows, filaments connecting the bundle to adjacent networks and notably transverse filaments (colour-coded in blue by their orientation). N=2 experiments. **b**, Cellular cryo-ET of the stress fibre. Left: a tomographic slice, of 6.8 nm thickness (Extended Data Fig. 5), showing the organization of actin filaments into a stress fibre and associated microtubules (MTs), indicated with white arrows. Right: 3D rendering of the actin filament network and microtubules (purple). Yellow arrow, plasma membrane. Blue arrows, lateral part of the bundle that is oriented towards the cytoplasm and where filament density is lower than in the inner part of the bundle. Scale bar, 200 nm. N=2 experiments. **c**, STORM reconstructed image of the actin network (Alexa Fluor 647 phalloidin) in an RPE1 cell plated on a dumbbell-shaped micropattern on a glass substrate (scale bar, 5 μm). The interlacing of the peripheral stress fibre with the surrounding actin cortex is highlighted in the yellow inset and associated zoomed-in image below (scale bar, 1 μm). N=1 experiment. **d**, STORM reconstructed image of the actin network of a rat astrocyte and a COS-7 cell and associated zoomed-in images of the yellow insets below. Scale bars, 5 μm. Zoomed-in scale bars, 1 μm. N=1 experiment. **e**, Top: immunostainings of phospho-myosin light chain in an RPE1 cell spread on a polyacrylamide dumbbell-shaped micropattern. Scale bar, 10 μm. Zoomed-in images of the yellow inset are displayed below for actin (phalloidin Atto 488) and p-MLC. For the p-MLC, the signal is displayed at saturation to highlight small myosin patches inside the actin mesh. Red arrows, area where actin structures are organized into bundles; red rectangles, areas devoid of actin-identifiable structures. Bottom: same with alpha-actinin. N=3 experiments.
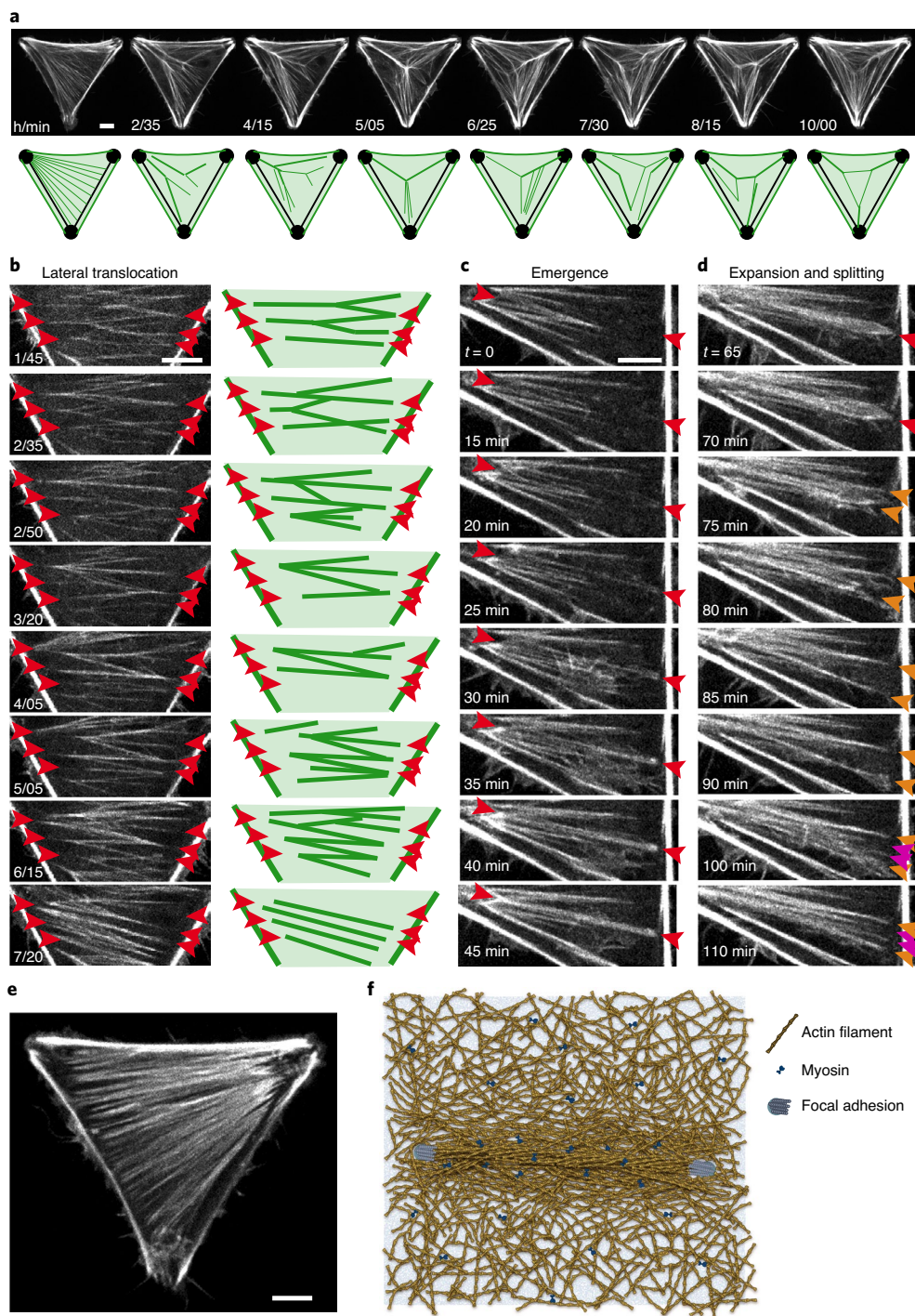
Fig. 6 | Emergence and translocation of cytoplasmic bundles in the cortical meshwork. a, Top row: live imaging of RPE1–LifeAct-GFP cells on tripod-shaped micropattern showing the global and permanent remodelling of the network architecture, suggestive of a complex interplay of longitudinal and lateral forces on cytoplasmic bundles (corresponding Supplementary Video 5). $N=1$ experiment. Scale bar, 10 μm. Bottom row: schematic representation of the dynamic reorganization of fibres. **b**, Left column: live imaging of RPE1–LifeAct-GFP cells on tripod-shaped micropattern highlighting network reconfiguration by lateral translocation of cytoplasmic bundles in the absence of anchorage displacement (red arrows; corresponding Supplementary Video 6). $N=1$ experiment. Scale bar, 10 μm. Right column: schematic representation of the dynamic reorganization of fibres. **c**, Live imaging of RPE1–LifeAct-GFP cells on tripod-shaped micropattern revealing the emergence of cytoplasmic bundles from the cortical meshwork (in between red arrows; corresponding Supplementary Video 7). $N=1$ experiment. Scale bar, 10 μm. **d**, Live imaging of RPE1–LifeAct-GFP cells on tripod-shaped micropattern showing the lateral expansion of a bundle (red arrow), its splaying into a wider structure (orange arrows) and its re-coalescence into several adjacent bundles (magenta arrows; corresponding Supplementary Video 7). $N=1$ experiment. Scale bar, 10 μm. **e**, RPE1–LifeAct-GFP cells on tripod-shaped micropattern displaying a dense and quasi-continuous network of cytoplasmic bundles. $N=1$ experiment. Scale bar, 10 μm. **f**, Schematic representation of the stress fibre anchored at its two edges on the substrate via focal adhesions (blue discs) as a fully embedded structure within the surrounding contractile actin cortex (myosins are represented by blue bow-ties). In all panels, time is indicated in hours and minutes.

cortex ranging from few aligned filaments to larger bundles of a few hundred nanometres. The zoomed-in view of the COS cell shows the alignment and incorporation of individual filaments, or bundles of a few filaments, at the end of a large bundle.

We then studied the similarities and differences in the structure and composition of the cortical meshwork and the stress fibres. Retinal-pigmented epithelial (RPE1) cells on the dumbbell-shaped micropattern were immunostained for phospho-myosin light chain (p-MLC) and alpha-actinin. With high-resolution confocal microscopy, although the density of actin filaments was lower in the region between the two stress fibres and appeared darker compared to the high intensity of the two fibres, a meshwork of bundles and filaments could be visualized at higher signal saturation, together with numerous patches of alpha-actinins and myosin (Fig. 5e, top). Consistent with this observation, the down-regulation of the expression of alpha-actinins increased the contraction of both the cortex and the stress fibres (Extended Data Fig. 3d). These observations confirmed that although their architectures were different, the stress fibres and the central mesh shared several key molecular players involved in the regulation of their contraction.

Live imaging further supported our conclusion of the stress fibres being embedded in the cortical meshwork. Cells were plated on a tripod-shaped micropattern in order to observe cytoplasmic network dynamics above a large non-adhesive area. Although cells were not moving, the actin network displayed a dramatic and permanent reorganization (Fig. 6a and Supplementary Video 6). This corroborated previous observations that cytoplasmic bundles can fuse with or split from the peripheral fibres[9,43–46] (Extended Data Fig. 6a). The mechanism supporting the remodelling of the network architecture, and in particular the lateral translocation of bundles, is still unclear. Longitudinal contractile forces, along the bundle, can promote the lateral translocation of curved bundles[9,46]. Interestingly, rather straight bundles were also capable of moving laterally and of fusing with and splitting from adjacent bundles (Fig. 6b). These movements happen in response to the production of lateral forces, normal to the bundle, without any translocation of their anchorages (arrows in Fig. 6b and Supplementary Video 7), suggesting that lateral forces were produced by the contractile meshwork between bundles, as recently suggested by others[47].

Interestingly, in regions of lower density of bundles, new bundles were found capable of emerging from the cortical meshwork (Fig. 6c and corresponding Supplementary Video 8, and Extended Data Fig. 6a). Without any visible splitting event from adjacent bundles, the new bundle appeared as a thin line of higher density forming first near a former attachment to the substrate and elongating towards a pre-existing bundle (time (t) $= 0$ to $t = 30$ min). Bundle thickening was homogeneous all along its length, suggesting further reinforcement by lateral recruitment of cortical filaments ($t = 30$ to $t = 45$ min). Interestingly, the newly formed bundle then expanded into a wider structure and eventually split into several bundles (indicated by orange arrows in Fig. 6d and Supplementary Video 8). This lateral expansion and splaying further supported the existence of lateral forces associated with the contractility of the adjacent cortical meshwork. The expansion and merging of bundles sometimes led to the assembly of a quasi-continuous structure in which individual bundles were almost impossible to distinguish (Fig. 6e)[47]. This showed that stress fibres not only were connected to the cortical meshwork but also could stem from the coalescence of filaments in the cortex, an assembly process that further accounts for their complete embedding in this meshwork (Fig. 6f).

Bundles appeared more static above an adhesive area than above a non-adhesive area (Extended Data Fig. 6b,c). This further suggested that the capacity to glide in the cortex helped the coalescence of thin bundles into larger stress fibres, whereas the presence of anchorages to the underlying extra-cellular matrix kept thin bundles static and separated. This absence of coalescence of small

bundles into larger fibres above adhesive regions could account for the lower energy release induced by bundle ablation in the pill-shaped as compared to the dumbbell-shaped micropatterns (Extended Data Fig. 6d) and for the difference in total cellular force production in geometries with various levels of non-adhesive area (Fig. 1c,d and Extended Data Fig. 1d).

Discussion

Our investigation of the force production by different actin networks revealed unexpected properties of the intracellular actomyosin machinery that appeared essential to integrate and transmit forces at the level of the cell. We demonstrated that the stress fibres are fully embedded in a contractile cortical actin network, and are not independent structures or structures with only discrete connections to other stress fibres. This meshwork of stress fibres and cortical filaments forms a mechanical continuum (Fig. 6f). Our conclusion agrees with the previous ultrastructural observations of the connections of the cortical-actin network to stress fibres and the more recent demonstration by electron microscopy that these connections depend on filamin A (refs. [21,48,49]). It also fits well with high-resolution imaging showing self-alignment of myosin II contractile ministacks in random meshworks[50] and lateral interactions of myofibrils, which support long-range self-organization of contractile structures[47,51]. Hence we found that contractile forces generated by the stress fibre are not only manifested at stress fibre anchorage points but also propagated across the entire cell via the cortical meshwork. Also, we demonstrated that the contraction of the cortical meshwork actively contributes to traction force transmission to focal adhesions, thereby impacting the overall magnitude of the contractile energy of the cell.

The mechanical interdependence of stress fibres and the cortical meshwork was supported by visualization of the network architecture in that filaments in the cortical meshwork tended to align with closer proximity to the stress fibre (Fig. 6f). This suggested that the randomly orientated filaments in the cortical network were converted into bundles of aligned filaments the nearer they were to the stress fibre, perhaps in a self-amplifying mechanism in which the bundle reinforces the tension in the stress fibre. We suspect this interconversion mechanism between the thin and non-attached filaments of the cortical network and bundled filaments to be essential for the rapid modulation of the production of traction forces, in response to changes of geometrical and mechanical cues.

Online content

Any methods, additional references, Nature Research reporting summaries, source data, extended data, supplementary information, acknowledgements, peer review information; details of author contributions and competing interests; and statements of data and code availability are available at https://doi.org/10.1038/s41563-020-00825-z.

References
1. Katoh, K., Kano, Y., Masuda, M. & Onishi, H. Isolation and contraction of the stress fiber. *Mol. Biol. Cell* **9**, 1919–1938 (1998).
2. Chrzanowska-Wodnicka, M. & Burridge, K. Rho-stimulated contractility drives the formation of stress fibers and focal adhesions. *J. Cell Biol.* **133**, 1403–1415 (1996).
3. Naumanen, P., Lappalainen, P. & Hotulainen, P. Mechanisms of actin stress fibre assembly. *J. Microsc.* **231**, 446–454 (2008).
4. Chugh, P. et al. Actin cortex architecture regulates cell surface tension. *Nat. Cell Biol.* **19**, 689–697 (2017).
5. Chugh, P. & Paluch, E. K. The actin cortex at a glance. *J. Cell Sci.* **131**, jcs186254 (2018).
6. Livne, A. & Geiger, B. The inner workings of stress fibers—from contractile machinery to focal adhesions and back. *J. Cell Sci.* **129**, 1293–1304 (2016).

7. Kurzawa, L. et al. Dissipation of contractile forces: the missing piece in cell mechanics. *Mol. Biol. Cell* **28**, 1825–1832 (2017).

8. Burridge, K. & Guilluy, C. Focal adhesions, stress fibers and mechanical tension. *Exp. Cell Res.* **343**, 14–20 (2016).

9. Hotulainen, P. & Lappalainen, P. Stress fibers are generated by two distinct actin assembly mechanisms in motile cells. *J. Cell Biol.* **173**, 383–394 (2006).

10. Schulze, N. et al. FHOD1 regulates stress fiber organization by controlling the dynamics of transverse arcs and dorsal fibers. *J. Cell Sci.* **127**, 1379–1393 (2014).

11. Tojkander, S., Gateva, G. & Lappalainen, P. Actin stress fibers – assembly, dynamics and biological roles. *J. Cell Sci.* **125**, 1855–1864 (2012).

12. Tojkander, S., Gateva, G., Husain, A., Krishnan, R. & Lappalainen, P. Generation of contractile actomyosin bundles depends on mechanosensitive actin filament assembly and disassembly. *Elife* **4**, e06126 (2015).

13. Burnette, D. T. et al. A role for actin arcs in the leading-edge advance of migrating cells. *Nat. Cell Biol.* **13**, 371–382 (2011).

14. Shemesh, T., Verkhovsky, A. B., Svitkina, T. M., Bershadsky, A. D. & Kozlov, M. M. Role of focal adhesions and mechanical stresses in the formation and progression of the lamellipodium-lamellum interface [corrected]. *Biophys. J.* **97**, 1254–1264 (2009).

15. Wang, N., Butler, J. P. & Ingber, D. E. Mechanotransduction across the cell surface and through the cytoskeleton. *Science* **260**, 1124–1127 (1993).

16. Hu, S. et al. Intracellular stress tomography reveals stress focusing and structural anisotropy in cytoskeleton of living cells. *Am. J. Physiol. Cell Physiol.* **285**, C1082–C1090 (2003).

17. Cai, Y. et al. Cytoskeletal coherence requires myosin-IIA contractility. *J. Cell Sci.* **123**, 413–423 (2010).

18. Tanner, K., Boudreau, A., Bissell, M. J. & Kumar, S. Dissecting regional variations in stress fiber mechanics in living cells with laser nanosurgery. *Biophys. J.* **99**, 2775–2783 (2010).

19. Kumar, S. et al. Viscoelastic retraction of single living stress fibers and its impact on cell shape, cytoskeletal organization, and extracellular matrix mechanics. *Biophys. J.* **90**, 3762–3773 (2006).

20. Chang, C.-W. & Kumar, S. Vinculin tension distributions of individual stress fibers within cell-matrix adhesions. *J. Cell Sci.* **126**, 3021–3030 (2013).

21. Kumar, A. et al. Filamin A mediates isotropic distribution of applied force across the actin network. *J. Cell Biol.* **218**, 2481–2491 (2019).

22. Kassianidou, E., Brand, C. A., Schwarz, U. S. & Kumar, S. Geometry and network connectivity govern the mechanics of stress fibers. *Proc. Natl Acad. Sci. USA* **114**, 2622–2627 (2017).

23. Smith, M. A. et al. A zyxin-mediated mechanism for actin stress fiber maintenance and repair. *Dev. Cell* **19**, 365–376 (2010).

24. Chapin, L. M., Blankman, E., Smith, M. A., Shiu, Y. & Beckerle, M. C. Lateral communication between stress fiber sarcomeres facilitates a local remodeling response. *Biophys. J.* **103**, 2082–2092 (2012).

25. Rossier, O. M. et al. Force generated by actomyosin contraction builds bridges between adhesive contacts. *EMBO J.* **29**, 1055–1068 (2010).

26. Stachowiak, M. R. & O'Shaughnessy, B. Recoil after severing reveals stress fiber contraction mechanisms. *Biophys. J.* **97**, 462–471 (2009).

27. Luo, Y., Xu, X., Lele, T. P., Kumar, S. & Ingber, D. E. A multi-modular tensegrity model of an actin stress fiber. *J. Biomech.* **41**, 2379–2387 (2008).

28. Besser, A., Colombelli, J., Stelzer, E. H. K. & Schwarz, U. S. Viscoelastic response of contractile filament bundles. *Phys. Rev. E* **83**, 051902 (2011).

29. Kassianidou, E. & Kumar, S. A biomechanical perspective on stress fiber structure and function. *Biochim. Biophys. Acta Mol. Cell Res.* **1853**, 3065–3074 (2015).

30. Guthardt Torres, P., Bischofs, I. & Schwarz, U. S. Contractile network models for adherent cells. *Phys. Rev. E* **85**, 011913 (2012).

31. Bischofs, I. B., Klein, F., Lehnert, D., Bastmeyer, M. & Schwarz, U. S. Filamentous network mechanics and active contractility determine cell and tissue shape. *Biophys. J.* **95**, 3488–3496 (2008).

32. Oakes, P. W., Banerjee, S., Marchetti, M. C. & Gardel, M. L. Geometry regulates traction stresses in adherent cells. *Biophys. J.* **107**, 825–833 (2014).

33. Linsmeier, I. et al. Disordered actomyosin networks are sufficient to produce cooperative and telescopic contractility. *Nat. Commun.* **7**, 12615 (2016).

34. von Erlach, T. C. et al. Cell-geometry-dependent changes in plasma membrane order direct stem cell signalling and fate. *Nat. Mater.* **17**, 237–242 (2018).

35. Théry, M., Pépin, A., Dressaire, E., Chen, Y. & Bornens, M. Cell distribution of stress fibres in response to the geometry of the adhesive environment. *Cell Motil. Cytoskeleton* **63**, 341–355 (2006).

36. Mandal, K., Wang, I., Vitiello, E., Orellana, L. A. C. & Balland, M. Cell dipole behaviour revealed by ECM sub-cellular geometry. *Nat. Commun.* **5**, 5749 (2014).

37. Peterson, L. J. et al. Simultaneous stretching and contraction of stress fibers in vivo. *Mol. Biol. Cell* **15**, 3497–3508 (2004).

38. Colombelli, J. et al. Mechanosensing in actin stress fibers revealed by a close correlation between force and protein localization. *J. Cell Sci.* **122**, 1665–1679 (2009).

39. Strahs, K. R. & Berns, M. W. Laser microirradiation of stress fibers and intermediate filaments in non-muscle cells from cultured rat heart. *Exp. Cell Res.* **119**, 31–45 (1979).

40. Koonce, M. P., Strahs, K. R. & Berns, M. W. Repair of laser-severed stress fibers in myocardial non-muscle cells. *Exp. Cell Res.* **141**, 375–384 (1982).

41. Kassianidou, E. et al. Extracellular matrix geometry and initial adhesive position determine stress fiber network organization during cell spreading. *Cell Rep.* **27**, 1897–1909.e4 (2019).

42. Toro-Nahuelpan, M. et al. Tailoring cryo-electron microscopy grids by photo-micropatterning for in-cell structural studies. *Nat. Methods* **17**, 50–54 (2020).

43. Hirata, H., Tatsumi, H. & Sokabe, M. Dynamics of actin filaments during tension-dependent formation of actin bundles. *Biochim. Biophys. Acta* **1770**, 1115–1127 (2007).

44. Luo, W. et al. Analysis of the local organization and dynamics of cellular actin networks. *J. Cell Biol.* **202**, 1057–1073 (2013).

45. Muller, A., Muller, S., Nasufovic, V., Arndt, H.-D. & Pompe, T. Actin stress fiber dynamics in laterally confined cells. *Integr. Biol.* **11**, 175–185 (2019).

46. Chen, T. et al. Large-scale curvature sensing by directional actin flow drives cellular migration mode switching. *Nat. Phys.* **15**, 393–402 (2019).

47. Hu, S. et al. Long-range self-organization of cytoskeletal myosin II filament stacks. *Nat. Cell Biol.* **19**, 133–141 (2017).

48. Marek, L. F., Kelley, R. O. & Perdue, B. D. Organization of the cytoskeleton in square fibroblasts. *Cell Motil.* **2**, 115–130 (1982).

49. Svitkina, T. M. Ultrastructure of the actin cytoskeleton. *Curr. Opin. Cell Biol.* **54**, 1–8 (2018).

50. Fenix, A. M. et al. Expansion and concatenation of nonmuscle myosin IIA filaments drive cellular contractile system formation during interphase and mitosis. *Mol. Biol. Cell* **27**, 1465–1478 (2016).

51. Dasbiswas, K., Hu, S., Schnorrer, F., Safran, S. A. & Bershadsky, A. D. Ordering of myosin II filaments driven by mechanical forces: experiments and theory. *Philos. Trans. R. Soc. B* **373**, 20170114 (2018).

Methods

Preparation of micropatterned polyacrylamide gels. The preparation of patterned polyacrylamide hydrogels was performed according to the mask method previously described in the literature[52]. A quartz photomask was first cleaned through an oxygen plasma (AST Products, 200 W) for 3.5 min. Areas containing the patterns were then incubated with 0.1 mg ml⁻¹ poly(L-lysine)-graft-poly(ethylene glycol) (PLL-g-PEG) (JenKem Technology, ZL187P072) in 10 mM HEPES buffer, pH 7.4, for 30 min. After de-wetting, the mask was exposed under deep UV for 5 min. Next, patterns on the mask were incubated with a mix of 10 µg ml⁻¹ fibronectin (no. F1141, Sigma) and 20 µg ml⁻¹ fibrinogen–Alexa-Fluor-647 conjugate (no. F35200, Invitrogen) in 100 mM sodium bicarbonate buffer with pH of 8.4 for 30 min. A mix of acrylamide (8%) and bis-acrylamide solution (0.264%) (Sigma) corresponding to the experimental Young's modulus of 34.8 kPa was degassed for approximately 30 min, mixed with 0.2 µm PLL-g-PEG-coated fluorescent beads (Fluorosphere no. F8810, Life Technologies) and sonicated before addition of APS (ammonium persulfate) and TEMED (*N,N,N′,N′*-tetramethylethylenediamine). Then 25 µl of that solution was added on the micropatterned photomask, covered with a silanized coverslip (Silane, no. M6514, Sigma) and allowed to polymerize for 25 min before being gently detached in the presence of sodium bicarbonate buffer. Micropatterns were stored overnight in sodium bicarbonate buffer at 4 °C before plating cells.

Atomic force microscopy measurements of Young's modulus of acrylamide gels. Gel stiffness was measured through nano-indentation using an atomic force microscope (Bruker Nanoscope) mounted with silica-bead-tipped cantilevers (bead radius = 2.5 µm; nominal spring constant, 0.06 N m⁻¹; Novascan Technologies). The sensitivity of the photodiode to cantilever deflection was determined by measuring the slope of a force–distance curve when pressing the cantilever onto a glass coverslip. The force constant of the cantilever was determined using the thermal-noise method included in the Bruker Nanoscope software. For each acrylamide/bis-acrylamide ratio used in the traction force microscopy measurements, 27 force curves in 3 by 3 grids were acquired (2 µm spacing between points) at three different locations on the gels. Before and during indentation experiments, gels were kept in phosphate buffered saline (PBS). Stiffness values from force curves were obtained using the NanoScope analysis software, correcting for baseline tilt using the linear fitting option with the Hertz model and a Poisson ratio of 0.48 on the indentation curve.

Preparation of micropatterned glass slides. To increase the resolution of actin images, RPE1 cells were grown on glass micropatterns prepared as previously described in the literature[53]. Glass coverslips were spin-coated for 30 s at 3,000 r.p.m. with adhesion promoter TI PRIME (MicroChemicals), then heated for 5 min at 120 °C and spin-coated again for 30 s at 1,000 r.p.m. with 1% polystyrene in toluene (Sigma). Coverslips were then oxidized by plasma (FEMTO, Diener Electronics; 19 s, 30 W) and incubated for 30 min with 0.1 mg ml⁻¹ PLL-g-PEG (PLL20K-G35-PEG2K, JenKem) in 10 mM HEPES, pH 7.4. Dried coverslips were next exposed to deep UV (UVO cleaner, Jelight) through a photomask (Toppan) for 5 min. Coverslips were incubated for 30 min with 10 µg ml⁻¹ fibronectin (Sigma) and 20 µg ml⁻¹ fibrinogen–Alexa-Fluor-647 conjugate (Invitrogen) in PBS after UV exposure.

Cell culture. Human telomerase-immortalized RPE1 cells (Clontech) either expressing LifeAct-GFP or wild-type[54] were grown in a humidified incubator at 37 °C and 5% CO₂ in DMEM/F12 medium supplemented with 10% foetal bovine serum and 1% penicillin and streptomycin (GIBCO/Life Technologies). Cells were plated at approximately 15,000 cells ml⁻¹ on patterned polyacrylamide gels and left to spread for 3 to 4 h before imaging. The ARP2/3 complex was inhibited with CK-869 inhibitor (Sigma-Aldrich C9124, 50 µM). To down-regulate the expression of alpha-actinin, RPE1 cells were transfected with two sets of short interfering RNAs (siRNAs; Qiagen) using lipofectamine RNAi Max transfection reagent (Life Technologies) at a final concentration of 10 nM following the manufacturer's protocol. Strand sequences were as follows: ACTN4 siRNA, 5′-GCAGCAUCGUGGACUACAATT-3′ and ACTN1 siRNA, 5′-GCACCAUCAUGGACCAUUAUT-3′. COS-7 cells (ATCC CRL-1651) were cultured in DMEM (Gibco) supplemented with 2 mM GlutaMAX (Gibco), 50 units per ml⁻¹ penicillin, 50 µg ml⁻¹ streptomycin (Penstrep, Gibco) and 10% foetal bovine serum (Gibco)[55]. Rat hippocampal neurons were cultured on 18 mm coverslips at a density of 6,000 cm⁻¹ from embryonic day 18 pups[56] following established guidelines of the French Animal Care and Use Committee (French Law 2013–118 of 1 February 2013) and approval of the local ethics committee (agreement 2019041114431531-V2 no. 20242). In these neuronal cultures, a small number of astrocytes (glial cells) such as the one shown in Fig. 5 are present and were labelled and imaged.

Immunostaining and labelling. Cells were pre-permeabilized in 0.5% Triton X-100 in cytoskeleton buffer for 17 s for p-MLC and alpha-actinin staining and then rapidly fixed in 4% paraformaldehyde in cytoskeleton buffer with 10% sucrose at pH 6.1 for 15 min at room temperature. Cells were then washed twice with cytoskeleton buffer and incubated in a quenching agent of 0.1 M ammonium

chloride for 10 min. For all conditions, after fixation, the cells were washed then blocked with 1.5% bovine serum albumin for 45 min. The cells were incubated with appropriate dilutions of primary antibodies in PBS containing 1.5% bovine serum albumin and 0.1% Tween overnight at 4 °C in a humid chamber. For the primary antibodies, anti-phospho-myosin light chain 2 (no. 3671, Cell Signaling Technology), anti-alpha-actinin (no. 05–384, Merck Millipore, clone AT6/172) and anti-paxillin (no. 610051, BD Biosciences, clone 349) were used. After several washing steps, the coverslips were then incubated with secondary antibodies (Alexa Fluor antibodies, Invitrogen) diluted in PBS with 1.5% bovine serum albumin and 0.1% Tween for 1 h at room temperature in a humid chamber. After washing, Phalloidin FITC (no. P5282, Sigma) was incubated for 20 min. After washing, coverslips were then mounted onto slides using Prolong Gold antifade reagent containing DAPI for nuclei staining (no. P36935, Invitrogen). Fluorescent TetraSpeck microspheres of 0.5 µm diameter (no. T7281, Life Technologies) were in some cases incubated with the coverslip to provide an internal fluorescence intensity reference. Whenever needed, SiR-actin (SC001, Spirochrome) was used at a concentration of 500 nM for 3 h to stain actin in living cells.

STORM imaging. After fixation and immunolabelling[55], cells were incubated with phalloidin–Alexa-Fluor-647 (0.5 µM, Thermo Fisher) overnight at 4 °C. After two quick rinses in phosphate buffer, RPE1 cells were mounted in a closed chamber in STORM buffer (Smart Kit, Abbelight) and imaged by STORM as described previously[57] using an N-STORM microscope (Nikon Instruments) equipped with an Ixon DU-897 camera (Andor) and controlled with Nikon Elements. Phalloidin (0.25 µM) was added in the STORM medium to mitigate progressive unbinding from actin filaments during imaging[55]. After locating a cell using low-intensity illumination, epifluorescence images were acquired in both the green and far-red channels. For STORM imaging of actin, the sample was continuously illuminated at 647 nm (full power) and a series of 60,000 to 100,000 images was taken (256 × 256 pixels, 15 ms exposure time). The N-STORM software (Nikon Instruments) was used for the localization of single fluorophore activations. After filtering localizations with more than 800 photons, the list of localizations was exported as a text file and the ThunderSTORM plugin[58] of Fiji was used to generate reconstructions.

Image acquisition and photoablation. Images of the different immunostainings and high-resolution time-lapse images of actin dynamics on the pill- and dumbbell-shaped micropatterns were acquired on a confocal microscope, Zeiss LSM800, using a ×63 magnification objective (Zen Blue version 2). Staining of p-MLC, alpha-actinin and paxillin were imaged using an AiryScan detector. GaAsP detectors were used for DAPI and micropattern stainings. Traction force mapping, together with regular RPE1–LifeAct-GFP, actin-GFP (CellLight Actin-GFP, BacMam 2.0 from Thermo Fischer Scientific) or SiR-actin (SC001, Spirochrome) imaging, were performed on a confocal spinning-disc system (EclipseTi-E Nikon inverted microscope equipped with a CSUX1-A1 Yokogawa confocal head, an Evolve EMCCD camera from Roper Scientific, Princeton Instruments). Photoablation was performed on a spinning-disc system from Nikon using the iLas2 device (Gataca Systems) equipped with a passively Q-switched laser (STV-E, ReamPhotonics) at 355 nm producing 500 picosecond pulses. Laser displacement, exposure time and repetition rate were controlled via ILas software interfaced with MetaMorph (Universal Imaging Corporation). Laser photoablation and subsequent imaging were performed with a CFI S-Fluor 100X/1.30 Oil objective (MRH02900, Nikon) or a CFI S-Plan Fluor 60X/0.7 ELWD objective. The laser power delivered before the objective, measured in the same conditions as that used to perform the photoablation experiment, was around 0.5 mW at 100% laser. According to the specifications of the objectives used, this corresponds approximately to 250 µW delivered at the output of the objective. The stress fibre punctual photoablation was performed on the fly during live acquisition. For the stress fibre shaving, photoablation was performed on a narrow region medial and parallel to the length of the fibre above the non-adhesive substrate on the hydrogel. In this case, 13 repetitions of 25 ms pulses were used with 100% of the 355 nm laser power, corresponding to a pulse of approximately 450 ms. Cells showing leakage or local blebbing following ablation were excluded from the analysis.

Measurement of cell traction forces with ImageJ. Data were analysed with a set of macros in Fiji using the method previously described in the literature[59]. Displacement fields were obtained from fluorescent bead images before and after removal of cells by trypsin treatment. Bead images were first paired and aligned to correct for experimental drift. The displacement field was calculated by particle imaging velocimetry on the basis of normalized cross-correlation following an iterative scheme. Final vector-grid size ranged from 1.55 µm × 1.55 µm to 1.60 µm × 1.60 µm depending on magnification. Erroneous vectors were discarded owing to their low correlation value and replaced by the median value of the neighbouring vectors. The traction force field was subsequently reconstructed by Fourier-transform traction cytometry, with a regularization parameter set to 8 × 10⁻¹¹. Force vectors located outside of the micropattern area were discarded. For the force quadrant analysis, the cell traction force was computed as above. The traction force field was divided into four zones using the two planes of symmetry of the dumbbell shape of the micropattern. In each zone, forces were summed up vectorially.

Cryo-electron tomography of micropatterned cells. Gold mesh grids overlaid with a perforated (R1/4) SiO_2 film (Quantifoil Micro Tools) were micropatterned using a one-step passivation and illumination based on a digital micromirror device, combined with a photo-activator, as previously described[42,60] (Leonardo v4.12, Alveole Lab). RPE1 cells were seeded on fibronectin micropatterned grids at a density of 8×10^3 cells per cm² for 20–35 min. Next, grids were transferred to a cell-free dish and incubated at 37 °C with 5% CO_2 to allow cell adhesion. Cells were vitrified 4–7 h post-transfer. Grids were blotted from the back side of the grid support film and immediately plunged into liquid ethane at liquid nitrogen temperature using a Leica EM GP plunger (Leica Microsystems). Cell thinning and imaging are described in the Supplementary Methods.

Statistical analysis. Statistical analysis and chart design were performed using Graphpad Prism 6 and R version 3.4.0 together with RStudio version 1.0.143.

Reporting summary. Further information on research design is available in the Nature Research Reporting Summary linked to this article.

Data availability
Raw data are available from the corresponding authors upon request. Source data are provided with this paper.

Code availability
Code is available from the corresponding authors upon request.

References

52. Vignaud, T., Ennomani, H. & Théry, M. Polyacrylamide hydrogel micropatterning. *Methods Cell Biol.* **120**, 93–116 (2014).
53. Azioune, A., Carpi, N., Tseng, Q., Théry, M. & Piel, M. Protein micropatterns: a direct printing protocol using deep UVs. *Methods Cell Biol.* **97**, 133–146 (2010).
54. Vignaud, T. et al. Reprogramming cell shape with laser nano-patterning. *J. Cell Sci.* **125**, 2134–2140 (2012).
55. Jimenez, A., Friedl, K. & Leterrier, C. About samples, giving examples: optimized single molecule localization microscopy. *Methods* **174**, 100–114 (2020).
56. Vassilopoulos, S., Gibaud, S., Jimenez, A., Caillol, G. & Leterrier, C. Ultrastructure of the axonal periodic scaffold reveals a braid-like organization of actin rings. *Nat. Commun.* **10**, 5803 (2019).
57. Ganguly, A. et al. A dynamic formin-dependent deep F-actin network in axons. *J. Cell Biol.* **210**, 401–417 (2015).
58. Ovesný, M., Křížek, P., Borkovec, J., Švindrych, Z. & Hagen, G. M. ThunderSTORM: a comprehensive ImageJ plug-in for PALM and STORM data analysis and super-resolution imaging. *Bioinformatics* **30**, 2389–2390 (2014).
59. Martiel, J.-L. et al. Measurement of cell traction forces with ImageJ. *Methods Cell Biol.* **125**, 269–287 (2015).
60. Engel, L. et al. Extracellular matrix micropatterning technology for whole cell cryogenic electron microscopy studies. *J. Micromech. Microeng.* **29**, 115018 (2019).

Acknowledgements

Author contributions
T.V. and L.K. performed most of the experiments. Q.T. performed preliminary work related to fibre ablation and traction force microscopy. C.C. and A.M. conceived and ran the model. C.L. performed STORM imaging. M.T.-N. and J.M. performed the Cryo-ET experiments. L.B., A.M., M.T. and L.K. designed the experiments, supervised the project and analysed data.

Competing interests
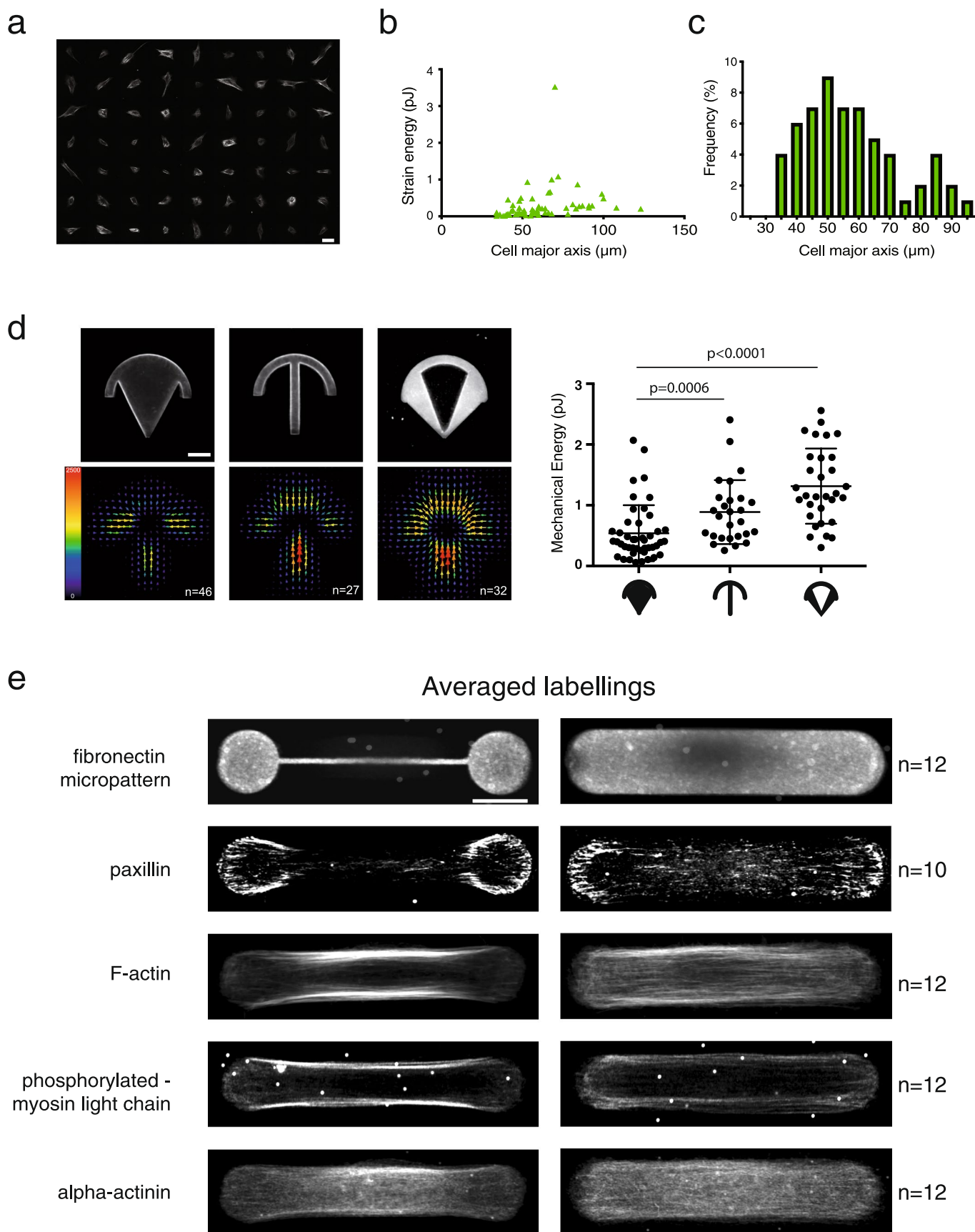The authors declare no competing interests.

Additional information
Extended data is available for this paper at https://doi.org/10.1038/s41563-020-00825-z.

Supplementary information is available for this paper at https://doi.org/10.1038/s41563-020-00825-z.

Correspondence and requests for materials should be addressed to A.M., M.T. or L.K.

Reprints and permissions information is available at www.nature.com/reprints.

a

b

c

d

e

Averaged labellings

fibronectin micropattern

paxillin

F-actin

phosphorylated - myosin light chain

alpha-actinin

n=12

n=10

n=12

n=12

n=12

Extended Data Fig. 1 | See next page for caption.

Extended Data Fig. 1 | Variations of contractility with cell shape and architecture. a. Actin filaments staining (SirActin 1 μM) of RPE1 live cells on homogeneous (non-micropatterned) fibronectin-coated polyacrylamide gels. N = 1 experiment. Scale bar=50 μm. **b**. Variation of the strain energy associated to cell traction forces with respect to the length of non-micropaterned cells. n = 63 cells, N = 1 experiment. **c**. Distribution of the length of RPE1 cells on homogeneous (non-micropatterned) poly-acrylamide gels. **d**. Traction-force maps of cells spread on various micropattern shapes. Upper images display the fibronectin coating on the micropatterns, and lower images show averaged traction-force maps of cells (scale colour bar in Pa). n-plain crossbow=46 cells, n-regular crossbow=27 cells, n-empty crossbow=32 cells, N = 1 experiment. The graph shows the scatter plot of the mechanical energies on each micropattern and associated p-value (mean and standard deviation are depicted, two-tailed Mann-Whitney t-tests, P = 0.0006 between plain and regular crossbow, P < 0.0001 between regular and empty crossbow). 2 outliers were automatically removed from the analysis (remove outliers function of Prism). **e**. Averaged localization of molecular components involved in cell contractility for cells displaying either two main peripheral stress fibers (when plated on dumbbell-shaped micropattern, left) or a continuous actin mesh (when plated on pill-shaped micropattern, right). For each shape, averaged Z projections of cells are displayed. From top to bottom: micropatterns labeling (fibrinogen–Cy5); paxillin (alexa-488); actin (phalloidin-ATO-488); phospho-MLC (CY3); alpha-actinin (CY3). Image scale bar = 10 μm. N = 3 experiments.
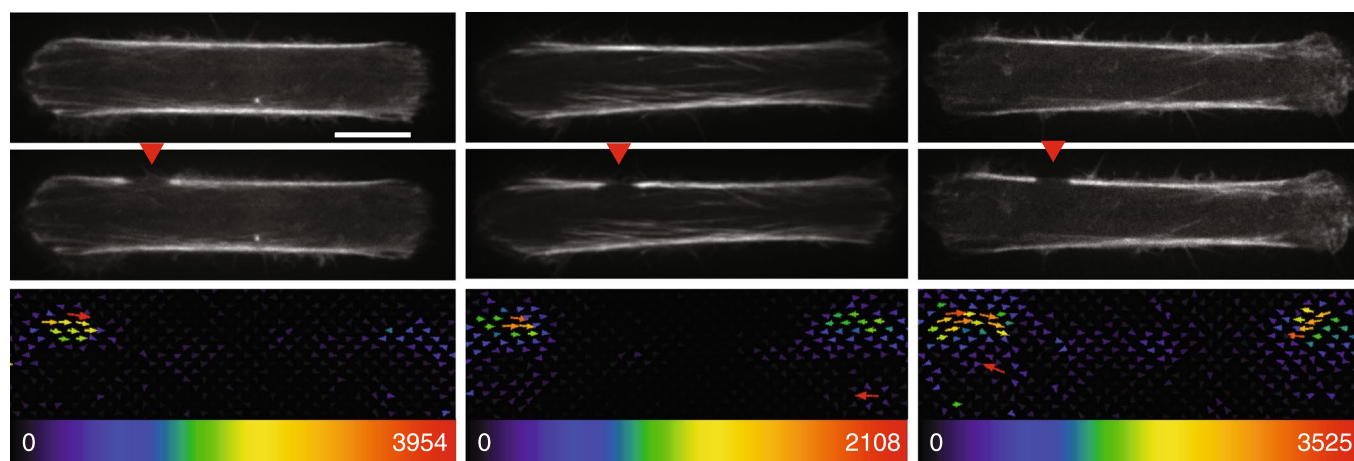
Extended Data Fig. 2 | Asymmetric force relaxation after an off-centered stress fiber cut. Images of RPE1-LifeAct-GFP cells before and after off-centered photoablation of the stress fiber (red arrow) and associated traction stress maps. Image scale bar = 10 μm. Force scale colour bar in Pa. N = 3 experiments.
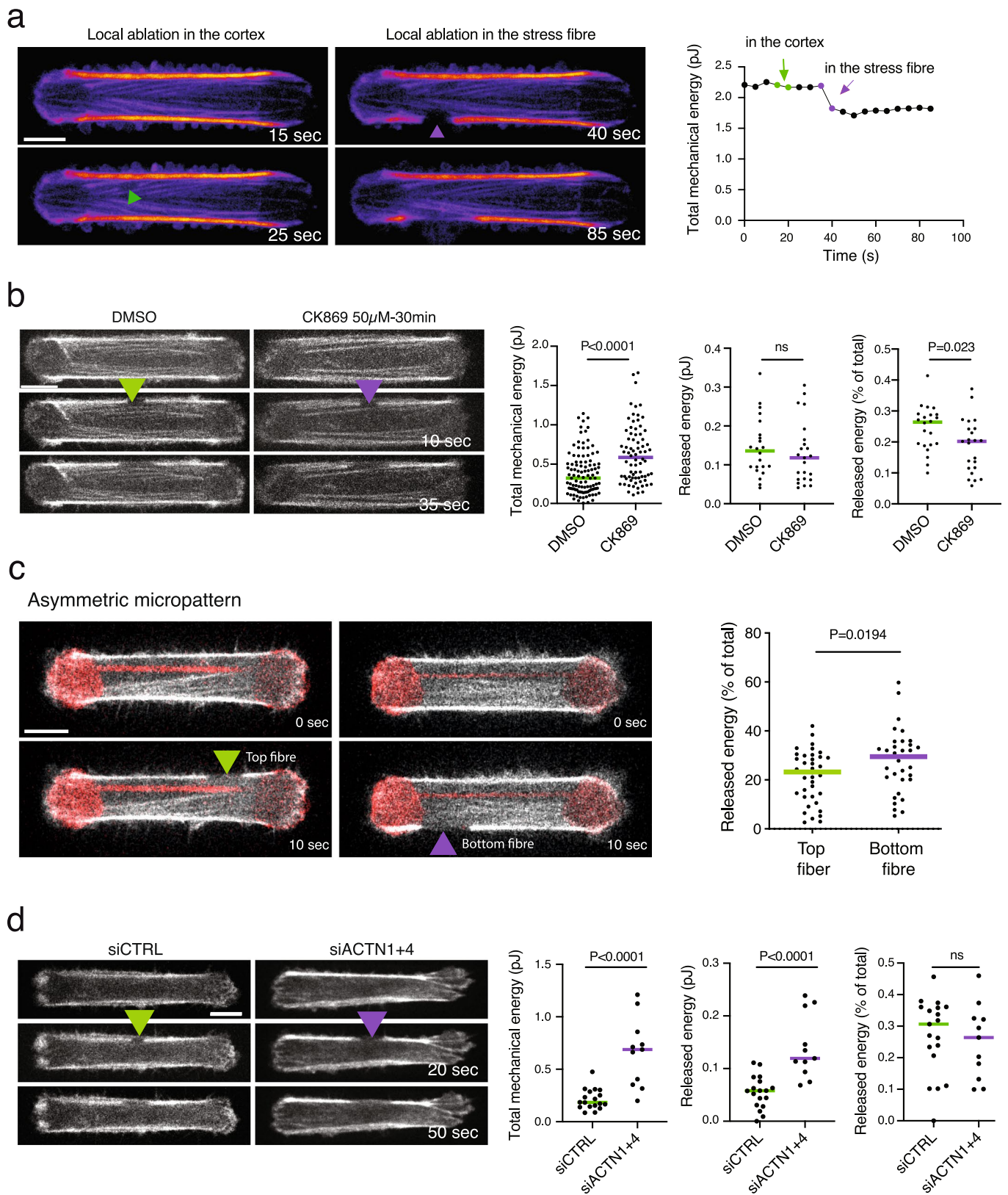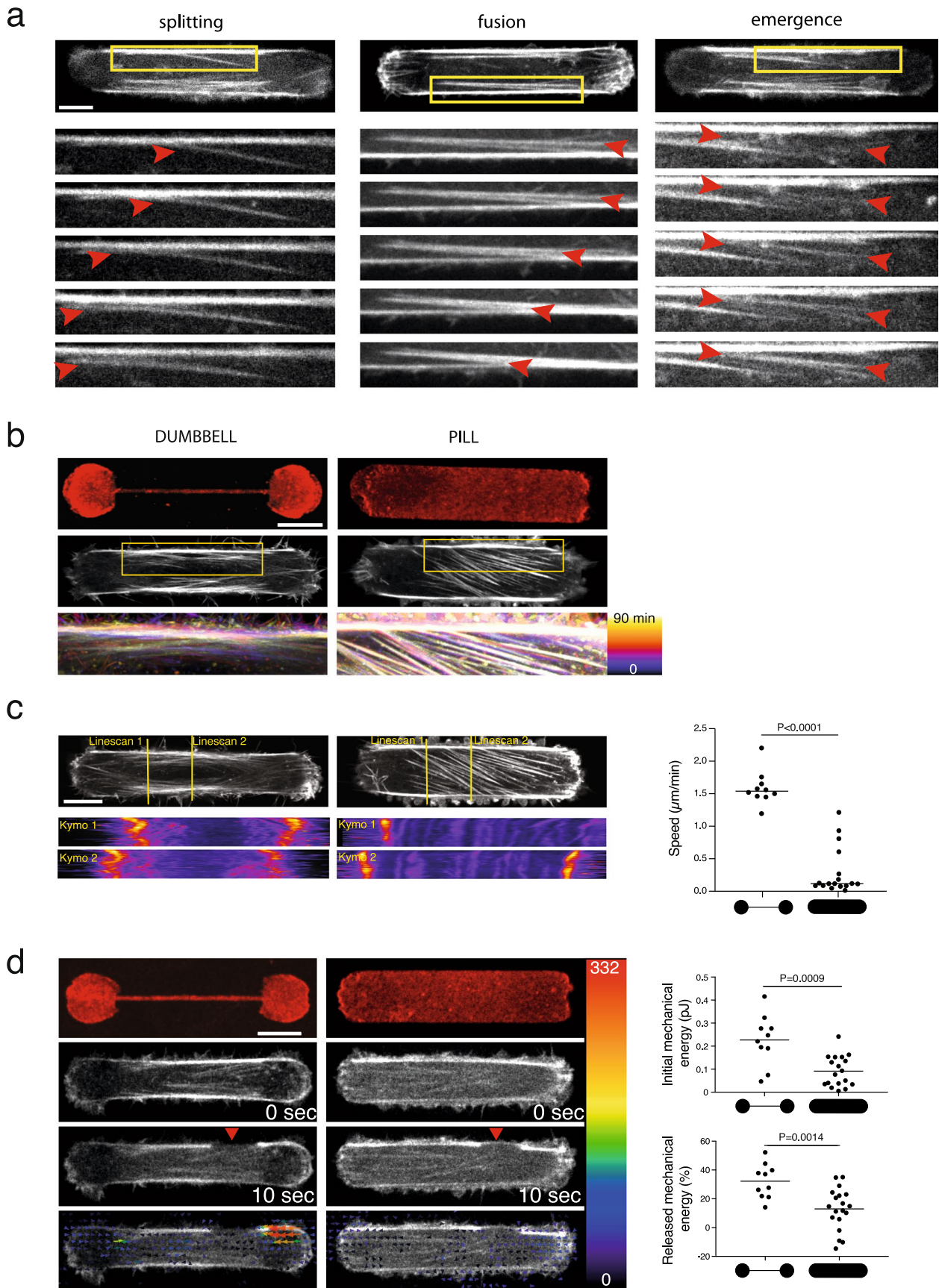
Extended Data Fig. 3 | See next page for caption.

Extended Data Fig. 3 | Regulation of the contributions of the cortex and the peripheral stress fibers to the total force. a. Comparison of the relative releases of strain energy following a single local ablation in the cortical meshwork (green arrowhead) or in the peripheral stress fiber (purple arrowhead). n=1 cell, N=1 experiment. **b**. Measurement of the total strain energy and the released energy following stress fiber ablation in control cells and cells treated with the Arp2/3 inhibitor CK869 (50 µM, 30 min). The total energy was increased in response to CK869, but the ablation of the fiber did not release more energy than in the control case, suggesting that the global increase was due to the hyper-contraction of the cortical network. In this experiment, cells from 2 different sizes (59 and 64 µm) were analyzed. For total mechanical energy: nDMSO=105 cells, nCK869=76 cells; N=3 experiments; p-value from unpaired t-test is indicated on the plot (P<0.0001). For ablation: nDMSO=22 cells, nCK869=23 cells; N=1 experiment. Statistical significance and p-value from a two-tailed paired t-test is indicated on the plot (P=0.5 for released energy; P=0.023 for relative released energy). Medians are depicted. 7 outliers were automatically excluded from the analysis for the initial energy plot and 1 for the ablation plots (remove outliers function of Prism). **c**. Releases of strain energy following a single ablation of peripheral stress fibers on asymmetric dumbbells (central bar off-centered by 2 µm). The top fiber was connected to a small area of cortex, spaning the space between the fiber and the anchorage on the bar. The bottom fiber was connected to a larger cortical network. The ablation of the bottom fiber released more contractile energy. nTop fiber=38, nBottom fiber=35; N=3 experiments, median is depicted. 2 cells for which stress fiber ablation was not efficient were eliminated from the analysis. p-value from two-tailed unpaired t-test is indicated on the plot (P=0.0194). 2 outliers were automatically excluded from the analysis (remove outliers function of Prism). **d**. Measurement of the total strain energy and the released energy following stress fiber ablation in cells treated with a control siRNA or with siRNA against apha-actin1 and actinin4. Down-regulation of alpha-actinins increased the total contractile energy, as well as the energy released by fiber ablation. The ratio between the two was not affected, suggesting that the contraction of the cortex increased as well. In this experiment, cells from 2 different sizes (59 and 64 µm) were analyzed. For total and released mechanical energy: n-siCTRL=18 cells, n-siACTN1+4=11 cells, for released mechanical energy % of total: n-siCTRL=19 cells, n-siACTN1+4=11 cells; N=1 experiment. p-values from two-tailed unpaired t-tests are indicated on the plots (P<0.0001 for initial and released energy, P=0.6678 for relative released energy). 1 oulier was automatically excluded from the analysis (remove outlier function of Prism).
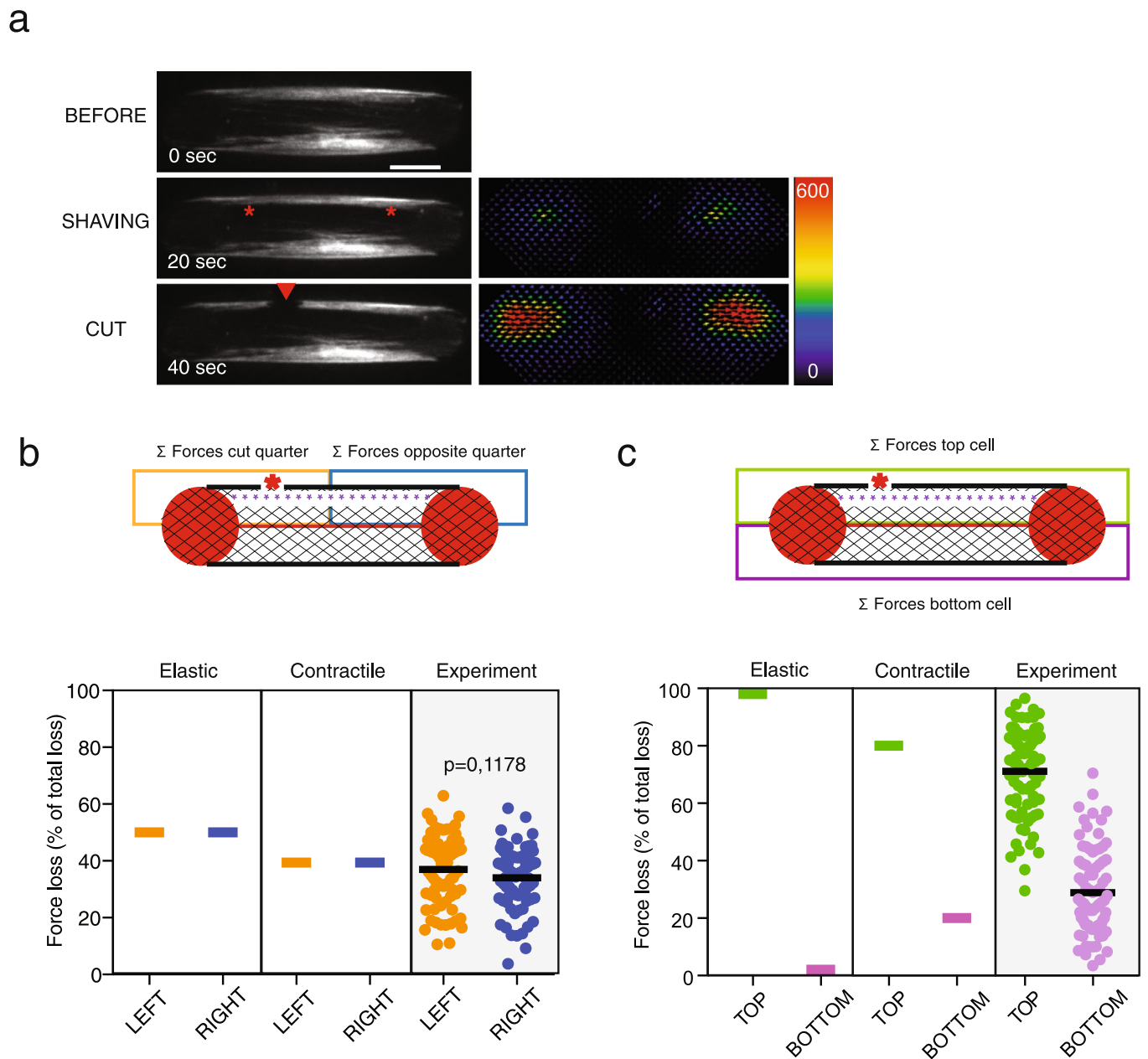
Extended Data Fig. 4 | Elastic and contractile model predictions of the force loss distribution after stress fiber shaving and photoablation. a. From top to bottom: Images of a representative RPE1-LA-GFP cell depicting the precut cell; a shaving; a consecutive cut together with the associated forces relaxed upon photoablation on the right panel. Image scale bar = 10 μm. Force scale colour bar in Pascal. N = 3 experiments. **b**. Spatial distribution of force loss along the stress fiber after stress-fiber shaving (purple dashed line) and off-center photoablation (red star). The loss of traction forces was calculated in partitioned area of the cell, where the orange zone included half the stress fiber and the off-centered photoablation site, and the blue zone included the other half of the stress fiber. Plot displaying the predictions of the elastic model, the contractile model and the experimental measurements (n = 80 cells, N = 14, mean is depicted). The p-value from a two-tailed paired t-test is indicated on the plot (P = 0.1178). **c**. Spatial distribution of force loss along the stress fiber after stress-fiber shaving (purple dashed line) and off-center photoablation (red star). The loss of traction forces was calculated in partitioned area of the cell, where the green zone included the stress fiber with photoablation site, and the purple zone included the stress fiber without photoablation. Plot displaying the predictions of the elastic model, the contractile model and the experimental measurements (n = 80 cells, N = 14, mean is depicted).
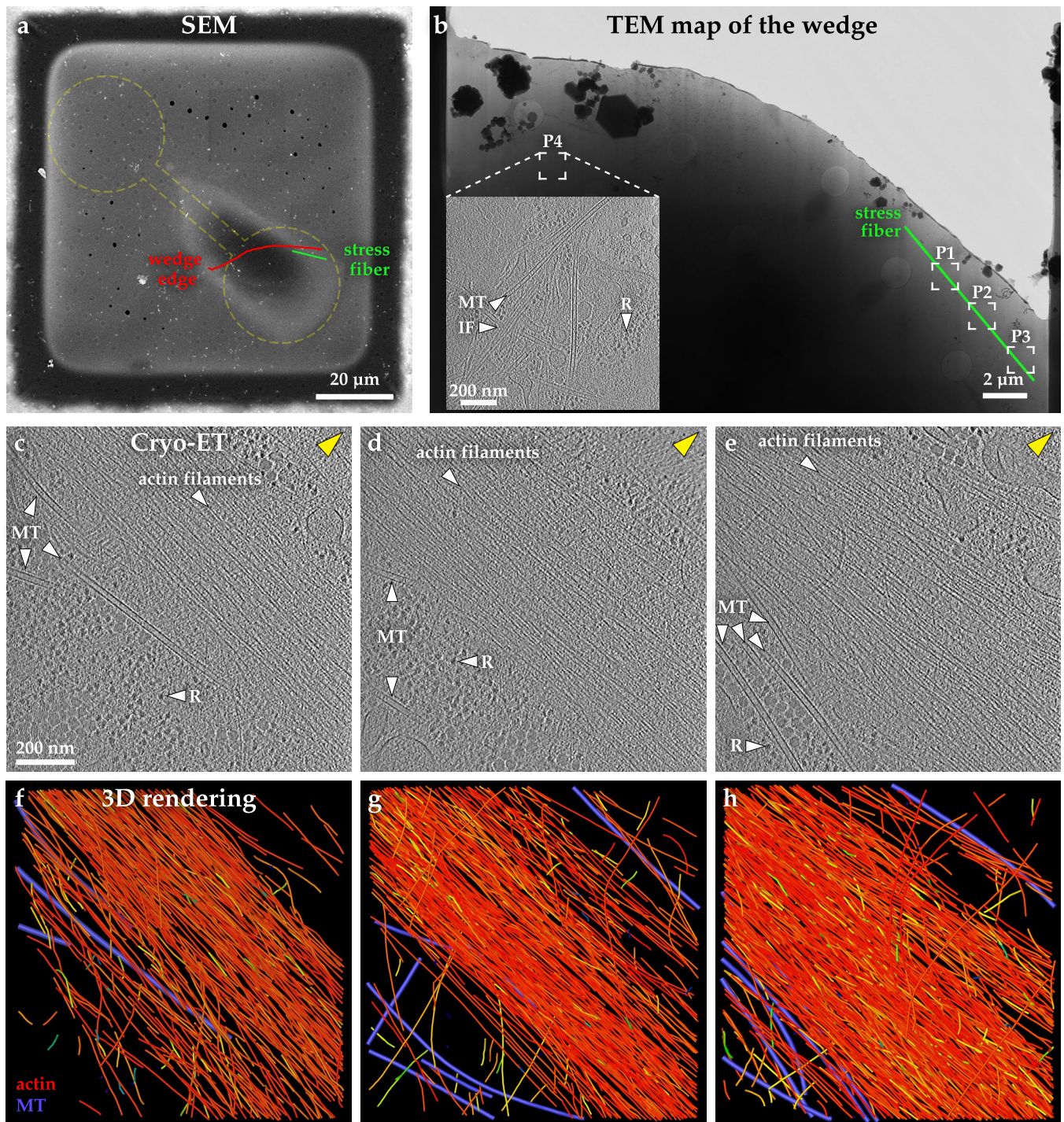
Extended Data Fig. 5 | Actin filament organisation in 3D within and near the stress fiber. a. Cryo-Scanning Electron Microscopy of a vitrified RPE1 cell adhered and spreading on a dumbbell-shape micropattern. Red line indicates the putative position of the edge of the wedge produced by cryo-FIB milling. The green line indicates the position of the stress fiber imaged by cryo-ET. The yellow dashed line represents the dumbbell shape pattern size and position. b. Cryo-TEM of the wedge of the RPE cell shown in (**a**), displaying the positions (P1-P4) for cryo-ET. Inset: 6.8 nm thick tomographic slice of the P4 region. Microtubules (MTs); ribosomes (R); intermediate filaments (IF). **c–e**. Cellular cryo-ET. Tomographic slices (6.8 nm thickness) of three positions - P1, P2 and P3 - in (**b**), respectively, along the same stress fiber. The three tomograms start at the basal membrane and extend the thickness of the tomograms towards the apical membrane. The distance between consecutive tomographed positions is ~ 2.5 μm (center-to-center of the tomograms), covering a total distance of ~7 μm. N = 2 experiments. **f–h**. 3D rendering of the actin filament network and microtubules (purple) from (**c–e**), respectively. Blue-to-red color map of actin filaments represent the angular distribution (ranging from 0° to 90°) relative to the z-plane of the tomogram. Most actin filaments are positioned parallel to the basal membrane. See related Video 5.

Extended Data Fig. 6 | See next page for caption.

Extended Data Fig. 6 | Dynamics and mechanics of cortical bundle fusion with lateral stress fibers depending on anchorage with the underlying extra-cellular matrix. a. Live imaging of RPE1-LifeAct-GFP cells on dumbbell-shaped micropattern revealing the splitting and fusion of cytoplasmic bundles with peripheral stress fibers (left and middle columns) as well as the emergence of cytoplasmic bundles from the cortical meshwork (right column at the red arrow heads) and its connection with peripheral stress fibers. Images from top to bottom show sequential acquisitions with a time frame of 10 min. N = 1 experiment. **b**. Color-coded overlay of sequential images acquired every 10 min on dumbbell-shaped (left) and pill-shaped micropatterns (right). Color overlay showed static structures in white and moving structures in colors ranging from blue to yellow depending on the time frame in which they were acquired. Scale bar=10 μm. **c**. Transversal linescans allowing the ploting of kymographs showing the transversal motion of internal actin bundles on dumbbell-shaped (left) and pill-shaped micropatterns (right). The graphs show the quantification of bundle velocity measured on the kymographs. n-dumbbell=18 actin paths, n-pill=10 actin paths; N = 1 experiment; median is depicted. Statistical significance of two-tailed unpaired t-test is indicated on the plot (P < 0.0001). **d**. Measurement of the total strain energy and the released energy following stress fiber ablation in cells plated on dumbbell-shaped (left) and pill-shaped micropatterns (right). Images show, from top to bottom: Micropattern labeling (fibrinogen–CY5); Actin before stress-fiber photoablation (0 sec) and after stress-fiber photoablation (10 sec); Overlay of the traction-force map and RPE1-LifeAct-GFP image after photoablation. Image scale bar = 10 μm. Graphs show the initial mechanical energy of the cells before the photoablation (top) and the released mechanical energy following photoablation of the peripheral stress fiber (% of the initial mechanical energy) (bottom). n = 10 cells for dumbbell and n = 18 cells for pill, N = 1 experiment, means are depicted. The p-values from two-tailed Mann-Whitney t-tests are indicated on the plots (P = 0.0009 for initial energy, P = 0.0014 for released energy).

Supplementary method

MODEL DESCRIPTION

The actin cytoskeletal meshwork is modeled as a two-dimensional deformable elastic material (Copos et al., 2017; Guthardt Torres et al., 2012; Kohler and Bausch, 2012; Zhu and Mogilner, 2012; Besser et al., 2011; Bischofs et al., 2008). This is a simplification of a three-dimensional model since on average the height of an adherent cell is much smaller than its in-plane dimensions, and so we neglect any out-of-plane deformations. The rheology of the cytoskeleton meshwork has been described as a viscoelastic gel with time-evolving material properties due to the turnover of actin and action of molecular motors (Moeendarbary et al., 2013; Mofrad, 2009; Gardel et al., 2008). There are two possible theoretical descriptions used to capture this rheology: (a) elastic elements embedded in a viscous gel (Barnhart et al., 2015; Larripa and Mogilner, 2006), or (b) viscous elements embedded in an elastic gel (Strychalski et al., 2015; Zhu and Mogilner, 2012; Joanny and Prost, 2009). The loss of traction force due to an ablation suggests that on timescales of tens of seconds the material response is well described by an elastic gel with viscous elements (Figure 1f). Further, it has been reported that the viscous timescale of the actin gel due to the growth and reorganization of actin filaments (order of minutes) is much longer than our observation time (Moeendarbary et al., 2013; Gardel et al., 2008).

For simplicity, the elastic gel is coarse-grained into a network of nodes interconnected by elastic springs, while viscous elements are excluded as their dynamics would only affect the transient behavior (Zhu and Mogilner, 2012; Zimmermann et al., 2010). An interconnected network of nodes and elastic links is a general theoretical approach used in previously published models to describe the mechanics of the cell interior of motile and adherent cells (Copos et al., 2017, Guthardt Torres et al., 2012; Zhu and Mogilner; 2012; Besser et al., 2011, Bischofs et al., 2008). While continuum approaches have been developed and successfully used as well (Barnhart et al., 2015; Oakes et al., 2014; Joanny and Prost, 2009), there is a tradition of modeling the cytoskeletal meshwork using discrete elements: nodes and springs (Boal, 2012).

Specifically, in the model, the cell interior is a two-dimensional rectangular network of nodes connected by Hookean elastic springs. The endpoints of the rectangular network are adhering to the substrate following experimental evidence (Figure 3a). The nodes represent material points of the cortical meshwork, while the elastic springs interconnecting the nodes model the mechanical response of the actin filament arrays. In the experiments with a dumbbell adhesive micropattern, large contractile actomyosin bundles are reported along the cell periphery stretching between the adhesive endpoints (Figure 1b). We include these bundles as additional nodes placed along a line at the top and bottom interface of the rectangular elastic meshwork. The nodes representing the actomyosin bundles are interconnected by Hookean elastic springs with an additional tension to mimic the effect of myosin-generated contractility. The nodes are also connected to the meshwork via additional linear elastic links. The endpoints of the contractile fibers are anchored to the substrate as was done with the endpoints of the elastic meshwork. Our theoretical model is similar in spirit to the model reported in (Paul et al., 2007):

in both models, the cortical meshwork is discretized into a network of interconnected nodes and deformable elements, however our elements are elastic, while in (Paul et al., 2007), these elements are not Hookean springs, but rather 'cables' – springs that do not respond to compression.

At the beginning of the simulation, the initial network of nodes and springs is the result of a Delaunay triangulation algorithm applied to a rectangular domain. The nodes are chosen to be the vertices of the triangulation and the elastic springs are along the edges of the triangulation. All springs are created in an undeformed state. The linear springs in the meshwork are characterized by a stiffness k_1, while the additional links representing the actomyosin bundles have spring stiffness k_2 and tension γ_2. The connectors between the contractile fibers and the elastic meshwork have the same spring stiffness as the meshwork k_1.

Given this initial shape, elastic forces are computed at every node in the network. As was done previously (Copos et al., 2017; Barnhart et al., 2015), we assume that adhesion complexes generate viscous resistance to the deformation of the meshwork. The respective resistive force is given by $\xi \vec{u}$ where ξ is the effective adhesion drag coefficient and $\vec{u}$ is the velocity of the network in the lab coordinate system. The adhesion resistive force is balanced by the active elastic stresses: $\xi \vec{u} = \vec{F}$ at every material point. The elastic force at the material point is denoted by $\vec{F}$. At each time step, elastic forces are computed in the entire meshwork and the velocity of each node is determined from the force balance. At the endpoints of the rectangular network, the velocity is enforced to be zero since the cell is adhering to the substrate at these locations. Once the position of the nodes is updated in time, elastic forces are re-computed at these new locations and the algorithm proceeds as indicated above. Because of the relatively small deformations we never observe instabilities or crossovers in the triangulation. When the network achieves mechanical equilibrium, the forces exerted by the meshwork on the substrate (i.e., at the endpoints) are recorded as traction forces and qualitatively compared with experiments.

The scope of this theoretical framework is to probe the respective contribution of actomyosin bundled stress fibers, the internal cortical meshwork, and their mechanical coupling on exerted traction forces. The investigation is achieved by qualitative comparison of model predictions of the spatiotemporal distribution of traction forces and experimental measurements from adherent cells.

The values of the parameters were not taken from the literature, as there is a great variation in mechanical parameters reported in the published data due to significant mechanical differences in cell types, states and mechanochemical environments, as well as in experimental assays reported in multiple publications. Rather, we obtained model parameters from fits to one part of the experimental data, specifically to the measured values of the force loss due to a single cut along a stress fiber and of the force loss due to ablation. The rest of the data shows very good

quantitative agreement with the predicted numerical experiments, without any additional changes in the parameter values (the number of parameters is also very small), which is a strong argument for the model validity. Moreover, as all measurements deal with the fraction of the force/energy loss, rather than with absolute dimensional force/energy values, we do not need the dimensional parameter values in the model. Rather, for computations, we normalize the parameters so that $k_1 = 1$ for the stiffness of the elastic network and the stiffness of the connections between the elastic meshwork and the contractile fibers.

For the contractile fibers we choose a larger spring stiffness of $k_2 = 20$ and tension $\gamma_2 = 2$ relative to the normalized stiffness of the elastic mesh. The value for the spring stiffness k_2 is chosen to qualitatively reproduce the force loss for two consecutive cuts along the same fiber; specifically, the difference in the force released between the two cuts would be less significant by increasing k_2. In the modified model with a contractile cortical meshwork, we found that decreasing k_2 results in too much force loss in the region the cell opposite of the injured stress fiber. The value for the tension in the stress fiber, γ_2, is arbitrarily chosen – numerical experiments have shown that we can reproduce the data by varying γ_2 in the wide range – but its value relative to γ_1 is important. First, indifferent of our numeric choices for the stress fiber parameters, k_2 and γ_2, in the absence of a tension in the meshwork (i.e., $\gamma_1 = 0$) ablation of the mesh would never produce a force loss (Figure 3g). Second, introducing too large of a tension in the meshwork would imply that cuts along the fiber release very little force. To introduce cortical tension, we set $\gamma_1 = 0.5 = 0.25\gamma_2$ to simultaneously reproduce the force loss due to a single cut along a stress fiber and force loss due to an ablation of the cortical network. In particular, there are two competing effects that limit the choice of γ_1 — increasing γ_1 increases the force released with ablation since the cortical mesh participates more in generating contraction, but increasing γ_1 decreases the force released with a single cut on the fiber as then, the stress fibers contributes more to the force of the entire system. To balance these competing effects and match the force loss in ablation and single cut observed in experiments, we fix $\gamma_1 = 0.25*\gamma_2$. Furthermore, we varied each of the two parameters, k_2, γ_2, individually, tenfold and chosen to match as close as possible the qualitative behavior seen in the experiments. The drag coefficient is 0.025 arbitrary force per velocity units (2 orders of magnitude smaller than the elastic forces). Because traction forces are computed after the meshwork relaxes to the equilibrium, the value of the drag coefficient does not affect our results. The timestep is $\Delta t = 0.0001$ arbitrary time units and is chosen to meet numerical stability constraints.

At each discretized location in the cortical meshwork, Newton's second law is the governing equation of the system:

$$\xi \vec{u} = \vec{F}$$

where ξ is the effective adhesion drag coefficient and $\vec{u}$ is the velocity in the lab coordinate system. The elastic force at every discretized location is represented by $\vec{F}$. For full transparency, we have made the code available on a public repository: XXX.

We introduced stochastic noise in the model by assuming that the parameters for tensions and elasticity in the network vary randomly in space. Specifically, these parameters (mechanical characteristics of each deformable element in the network) are independent random draws from standard normal distributions centered around the baseline value with some variance, e.g.

$$f(\gamma_1) = \frac{1}{\sigma\sqrt{2\pi}} e^{-\frac{1}{2}\left(\frac{x-\gamma_1^0}{\sigma}\right)^2}$$

where γ_1^0 is the baseline value for tension in the interior cytoskeletal mesh, and $\sigma = \gamma_1^0/3$ is the standard deviation. When this spatial noise is introduced in all parameters (both tensions and elasticities) in the entire network, we find that the qualitative trends observed in the deterministic model persist. Namely, less force is lost with shaving rather than a cut along a stress fiber, and a second consecutive cut along the same stress fibers results in less force loss on average. Similar results from simulations when the spatial mechanical noise is introduced only in elastic parameters (while contractility is constant), or only in contractile stresses (while elasticity is homogeneous).

Fig. 4d. single cut along SF   Fig. 4e. shaving   Fig. 4f. two cuts along same SF
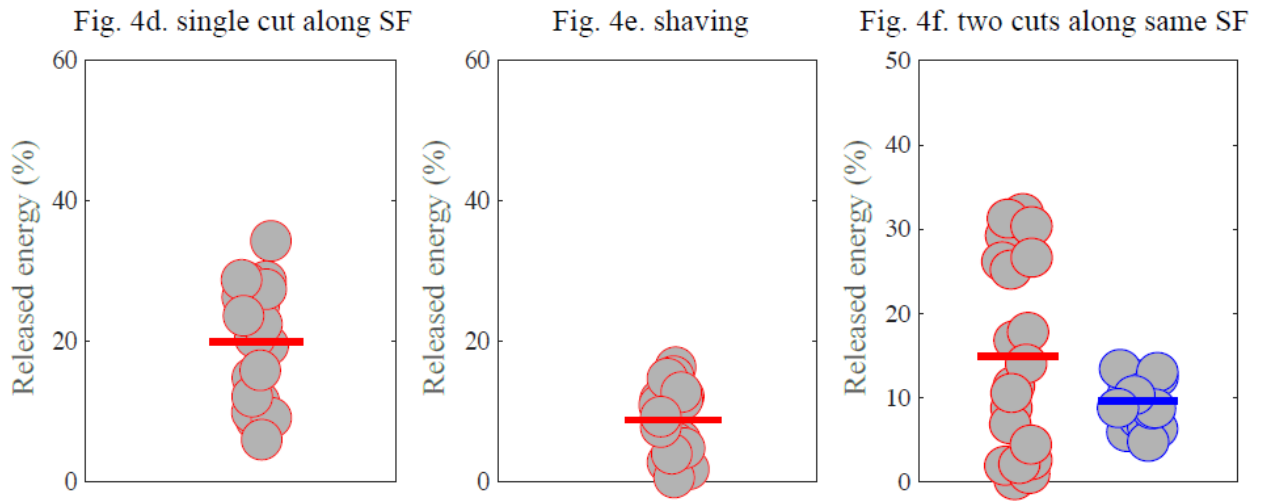
Statistics:

	Fig. 4d	Fig. 4e	Fig. 4f
mean	19.87%	8.80%	14.98% I 9.69%
standard deviation	8.30%	4.83%	11.51% I 2.50%
# samples	20	20	20

SUPPLEMENTARY REFERENCES

E. L. Barnhart, K.-C. Lee, G. M. Allen, J. A. Theriot, A. Mogilner. (2015) The balance between cell-substrate adhesion and myosin contraction determines the frequency of motility initiation in fish keratocytes. *Proc. Natl. Acad. Sci. USA* **112**: 5045-5050.

A. Besser, J. Colombelli, E. H. K. Stelzer, U. S. Schwarz. (2011) Viscoelastic response of contractile filament bundles. *Phys. Rev. E* **83**: 1-12.

I. B. Bischofs, F. Klein, D. Lehnert, M. Bastmeyer, U. S. Schwarz. (2008) Filamentous network mechanics and active contractility determine cell and tissue shape. *Biophys. J.* **95**: 3488-3496.

D. Boal. (2012) *Mechanics of the Cell*. Cambridge: Cambridge University Press.

C. A. Copos, S. Walcott, J. C. del Alamo, E. Bastounis, A. Mogilner, R. D. Guy. (2017) Mechanosensitive adhesion explains stepping motility in amoeboid cells. Biophys J, 112: 2672-2682.

M. L. Gardel, K. E. Kasza, C. P. Brangwyne, J. Liu, D. A. Weitz. (2008) Mechanical response of cytoskeletal networks. Methods Cell Biol. 89: 487-519.

P. Guthardt Torres, I. B. Bischofs, U. S. Schwarz. (2012) Contractile network models for adherent cells. *Phys Rev E* **85**: 011913.

J.-F. Joanny and J. Prost. (2009) Active gels as a description of the actin-myosin cytoskeleton. *HFSP J.* **3**: 94-104.

S. Kohler and A. R. Bausch. (2012) Contraction mechanisms in composite active actin networks. *PLoS One* **7**: e39869.

K. Larripa, A. Mogilner. (2006) Transport of a 1D viscoelastic actin-myosin strip of gel as a model of a crawling cell. *Physica A* **372**: 113-123.

E. Moeendarbary, L. Valon, M. Fritzsche, A. R. Harris, D. A. Moulding, A. J. Thrasher, E. Stride, L. Mahadevan, G. T. Charras. (2015) The cytoplasm of living cells behaves as a poroelastic material. *Nat Mat.* **12**: 253-261.

M. R. K. Mofrad. (2009) Rheology of the cytoskeleton. *Annu. Rev. Fluid Mech.* **41**: 433-453.

P. W. Oakes, S. Banerjee, M. C. Marchetti, M. L. Gardel. (2014) Geometry regulates traction stresses in adherent cells. *Biophys J.* **107**: 825-833.

R. Paul, P. Heil, J. P. Spatz, U. S. Schwarz. (2007) Propagation of mechanical stress through the actin cytoskeleton toward focal adhesions: model and experiment. *Biophys J.* **94**:1470-1482.

J. Zimmermann, M. Enculescu, M Falcke. (2010) Leading-edge gel coupling in lamellipodium motion. *Phys Rev E* **82**: 051925.

J. Zhu and A. Mogilner (2012) Mesoscopic model of actin-based propulsion. *PLoS Comp. Biol.* **8**: e1002764.